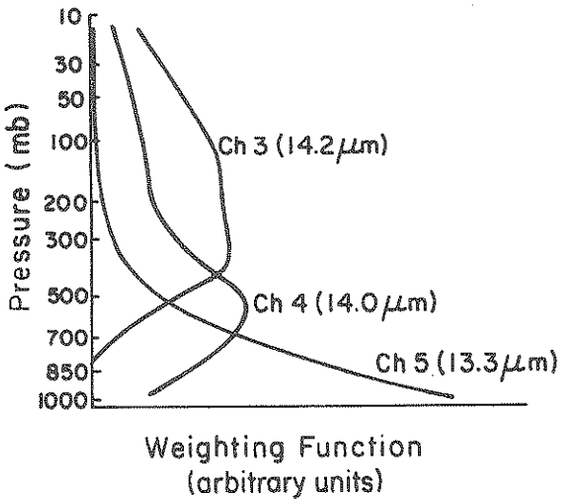

Figure 7.26 The weighting functions for three VAS CO_2 spectral bands centered at 14.2, 14.0, and 13.3 μm used in CO_2 slicing (Wylie and Menzel, 1989).

for the upwelling intensity at pressure level p. The radiation received at $p = 0$ then follows as[7]

$$I(0,\mu) = I(p,\mu)\mathcal{T}(p,0,\mu) + \int_0^p \mathcal{B}(p')\mathcal{W}(0,p')dp' \tag{7.55}$$

or in terms of the surface emission $I(p_s,\mu)$ as

$$I(0,\mu) = I(p_s,\mu)\mathcal{T}(p_s,p,\mu)\mathcal{T}(p,0,\mu) +$$

$$\mathcal{T}(p,0,\mu)\int_p^{p_s} \mathcal{B}(p')\mathcal{W}(p,p')dp' + \int_0^p \mathcal{B}(p')\mathcal{W}(0,p')dp' \tag{7.56}$$

With this form of transfer equation, it follows that the intensity difference between clear sky and a cloudy sky is

$$\Delta I = I_{clear} - I_{cldy} = \varepsilon \int_{p_s}^{p_c} \mathcal{T}(0,p')\frac{d\mathcal{B}(p')}{dp'}dp' \tag{7.57}$$

[7] There are a number of subtle assumptions in going from (7.54) to (7.56). The form of transfer equation given by (7.56) is referred to as the stacked layer equation. This is only valid when transmission functions multiply

$$\mathcal{T}(p_s,0,\mu) = \mathcal{T}(p_s,p,\mu)\mathcal{T}(p,0,\mu)$$

such as for transmission functions that are pure exponential functions of path.

where ε is the cloud emissivity and the wavelength ratio of this intensity difference defines a function

$$G(p_c) = \frac{\Delta I_1}{\Delta I_2} = \frac{\varepsilon_1 \int_{p_s}^{p_c} \mathcal{T}\frac{d\mathcal{B}_1}{dp'}dp'}{\varepsilon_2 \int_{p_s}^{p_c} \mathcal{T}\frac{d\mathcal{B}_2}{dp'}dp'}$$

that depends on cloud top pressure. This function is referred to as the cloud top pressure function and its general properties can be examined as follows. Suppose the optical depth of the atmosphere has the form

$$t(\tilde{p}) = \tau^*\tilde{p}^2 \tag{7.58}$$

which follows directly from (7.36) with $\tilde{p} = p/p_s$ and suppose also that the Planck function varies with pressure in the following simple way

$$\mathcal{B} = \mathcal{B}_o + \mathcal{B}^*\tilde{p}.$$

Substitution of (7.58) into the definition $\mathcal{T}(0,p) = \exp(-t(\tilde{p})/\mu)$ together with differentiation of the Planck function yields

$$G(p_c) = \frac{\mathcal{B}_1^* \int_{\tilde{p}_s}^{\tilde{p}_c} \tilde{p}' \exp[-\tau_1^*\tilde{p}'^2]d\tilde{p}'}{\mathcal{B}_2^* \int_{\tilde{p}_s}^{\tilde{p}_c} \tilde{p}' \exp[-\tau_2^*\tilde{p}'^2]d\tilde{p}'} \tag{7.59}$$

for $\mu = 1$. It is also convenient to assume that $\mathcal{B}_1^*/\mathcal{B}_2^* = 1$, that $\tilde{p}_s = p_s/p_o = 1$ and that the two wavelengths are close enough that $\varepsilon_1 = \varepsilon_2$. It follows from integration of (7.59) that

$$G(p_c) = \left(\frac{\tau_2^*}{\tau_1^*}\right)\frac{\exp[-\tau_1^*\tilde{p}_c^2] - \exp[-\tau_1^*]}{\exp[-\tau_2^*\tilde{p}_c^2] - \exp[-\tau_2^*]} \tag{7.60}$$

and examples of $G(p_c)$ derived from this formula are presented in Fig. 7.27a for different values of atmospheric optical depth τ_1^* and τ_2^*. The curves indicate how the cloud–top function depends on the ratio of optical depths as well as on the magnitude of these optical depths. In an optically thin atmosphere (curve 1), the function $G(p_c)$ only weakly depends on cloud–top pressure since emission by the clouds affects both channels more or less equally throughout most of the atmosphere. The other extreme is an optically thick atmosphere (curve 4) in which case the cloud–top pressure function is extremely sensitive to clouds with low cloud–top pressures. In this case, the peak of the weighting function of the optically thicker atmosphere

7

Passive Sensing — Emission

This chapter describes a theory of radiative transfer that includes the process of emission and introduces a number of remote sensing topics that are based on the measurement of this emission. Emission by the atmosphere is the source of atmospheric microwave and infrared radiation. We are able to deduce a great number of properties of the atmosphere from its measurement, including the amount and distribution of water vapor, the temperature profile, the amount of cloud liquid water, rainfall, and sea surface temperature.

Figure 7.1 is an example of a measured intensity spectrum obtained from the IRIS instrument flown on Nimbus 4. It provides a framework for thinking about how radiative transfer takes place in an absorbing–emitting atmosphere. Superimposed on the measured spectra are the blackbody curves for selected temperatures. Also highlighted are spectral positions of the absorption bands of the predominant absorbing gases. This diagram more clearly shows how emissions from different levels in the atmosphere (and therefore at different temperatures) combine to produce the observed spectra. For instance, emission in the central portions of the 9.6μm ozone band occurs at temperatures below about 250 K, and emission in the 15μm CO_2 band varies throughout the atmosphere according to the spectral position relative to the band center. For both O_3 and CO_2, the increase in emitted radiation in the center of the absorption band occurs higher up in the atmosphere than in the neighboring spectral regions where the absorption is weaker is indicative of the increase in temperature with increasing altitude in the stratosphere. Also noteworthy is the water vapor emission that is confined to the lower atmosphere (emission by the vibration and rotation bands is broadly characterized by the 275 K blackbody curve). An important spectral region is the atmospheric window between about 800 and 1200 cm^{-1} in which the atmosphere is almost transparent (except for the ozone band) and the emission originates from levels close to the surface. This spectral region is extensively used in remote sensing of surface and cloud properties as described shortly.

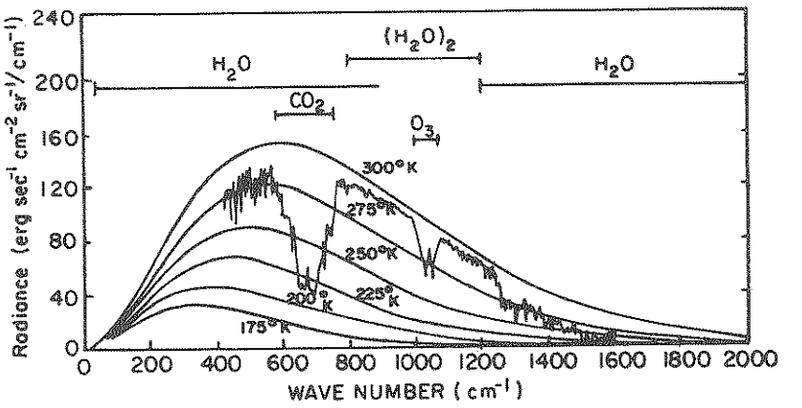

Figure 7.1 The infrared spectrum of radiation emitted from the atmosphere measured by the IRIS instrument. Shown are the blackbody curves derived for the different temperatures indicated as well as the principal absorbing gases that contribute to the spectrum (from Hanel, 1983).

7.1 Radiative Transfer with Emission

The increase of radiation along a path ds due to emission is

$$dI_\lambda = k_{\lambda,v} \mathcal{J}_\lambda ds \tag{7.1}$$

where $\mathcal{J}_\lambda$ is the *source function*. When this emission takes place in the lower atmosphere where thermodynamic equilibrium occurs, $\mathcal{J}_\lambda = \mathcal{B}_\lambda$. The net change in radiation along ds due to the combination of emission and extinction is

$$dI_\lambda = dI_\lambda(\text{emission}) + dI_\lambda(\text{extinction}) \tag{7.2}$$

It is reasonable to neglect scattering in many problems of infrared and microwave radiative transfer especially for clear sky conditions and, for most circumstances, for cloudy skies as well. Then substituting (6.1) and (7.1) in (7.2), we obtain the following transfer equation

$$\frac{dI_\lambda}{ds} = -k_{\lambda,v}[I_\lambda - \mathcal{B}_\lambda] \tag{7.3}$$

which is the mathematical relationship that describes how radiation is transferred from one layer to another layer as a result of absorption

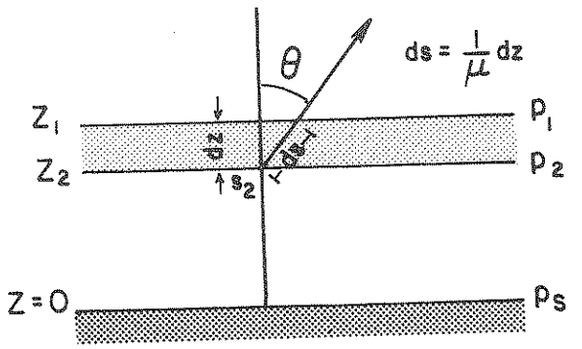

Figure 7.2 The geometric setting for the integral transfer equation in a plane parallel vertically stratified atmosphere.

and emission. The amount of radiation leaving the end of the path is a function of the distribution of absorber along the path (through the presence of $k_{\lambda,v}$) and the distribution of temperature (largely through the presence of $\mathcal{B}_\lambda$). We therefore expect that the measurement of intensity at the endpoint of the path contains information about both of these distributions. This is the principle upon which emission–based sounding of constituent concentration and temperature is based and this principle is a topic described in more detail later in this chapter.

The interactions between radiation and the gases of the atmosphere are generally weak enough that the photon mean free path is larger than the mean free path of molecules. Hence, the radiative transfer in the atmosphere tends to be nonlocal with significant contributions arising from different points along the path. This path–integrated emission is represented by the integral form of the radiative transfer equation. We obtain this equation by first making use of the definition, $d\tau_\lambda(s) = -k_{\lambda,v}(s)ds$, for an element of the optical thickness (the reason for the negative sign in this definition of optical thickness becomes evident later) and then multiply each side of (7.3) by the factor $\exp[-\tau_\lambda(s)]$. Combining terms gives

$$\frac{dI_\lambda e^{-\tau_\lambda(s)}}{d\tau_\lambda} = -\mathcal{B}_\lambda e^{-\tau_\lambda(s)} \tag{7.4}$$

Integration of this equation along a path extending from some point $s = s'$ to an end point $s = s''$ yields

$$I_\lambda(s'')e^{-\tau_\lambda(s'')} - I_\lambda(s')e^{-\tau_\lambda(s')} = \int_{\tau(s')}^{\tau(s'')} \mathcal{B}_\lambda(s)e^{-\tau_\lambda(s)}d\tau(s)$$

which, on rearrangement, gives

$$I(s'') = I(s')e^{-[\tau(s')-\tau(s'')]} + \int_{s'}^{s''} \mathcal{B}(s)e^{-[\tau(s)-\tau(s'')]}d\tau(s) \tag{7.5}$$

where the wavelength dependence of all factors in (7.5) is taken to be understood. The first term on the right–hand side of this equation represents the radiation, originally incident at s', that is transmitted to s''. We will refer to this as the surface term and describe one application where this term is used to obtain surface temperature. The integral term represents the emitted radiation from all points along the path and transmitted to s''.

When (7.5) is applied to the atmosphere, it is customary, but not necessarily realistic, to assume that the atmosphere is plane parallel and horizontally homogeneous. For such a stratified atmosphere, the integral equation (7.5) can be expressed in terms of optical depth $\tau(z)$ [rather than optical thickness $\tau(s)$]. It is conventional to define the optical depth such that $\tau = 0$ at the top of the atmosphere and $\tau = \tau^*$ at the surface.[1] For slant paths, the expression relating optical depth to optical path is

$$\tau(s) = \tau(z)/\cos\theta$$

producing

$$I(\tau, +\mu) = I(\tau^*, \mu)e^{-(\tau^*-\tau)/\mu} + \int_\tau^{\tau^*} \mathcal{B}(t)e^{-(t-\tau)/\mu}\frac{dt}{\mu} \tag{7.6a}$$

for $0 < \mu < 1$ which defines radiation that upwells from the atmosphere, and

$$I(\tau, -\mu) = I(0, -\mu)e^{-\tau/|\mu|} + \int_0^{\tau^*} \mathcal{B}(t)e^{-(\tau-t)/|\mu|}\frac{dt}{|\mu|} \tag{7.6b}$$

for $0 > \mu > -1$ for downwelling radiation.

[1] The convention that τ increases downward from the top of the atmosphere has roots in the traditional astrophysics literature on radiative transfer where τ is taken to increase along the direction of sunlight entering the atmosphere of distant planets. Optical depth increases in the opposite sense to z and hence the negative sign in its definition.

Excursus: The Angular Properties of Emitted Radiation

Consider an isothermal atmosphere with $\mathcal{B} = \mathcal{B}_o$ where $\mathcal{B}_o$ is a constant. Now imagine that a radiometer on the ground scans across the sky. The relevant equation that describes the radiation sensed by this instrument is (7.6b) which simplifies to

$$I(\tau^*; -\mu) = \mathcal{B}_o[1 - e^{-\tau^*/|\mu|}] \tag{7.7}$$

assuming that the cosmic term $I(0, -\mu) = 0$. This expression predicts that, for a given value of τ^*, the downwelling intensity is a minimum at $\mu = 1$ (directly downward), and increases to a value of $\mathcal{B}_o$ as the instrument scans out to the horizon. This increase is referred to as *limb brightening* and arises from the fact that the effective level of the emission decreases in the atmosphere as the zenith angle increases.

Consider the same instrument on a satellite and suppose it scans as it looks down at Earth. Again for an isothermal atmosphere, direct integration of (7.6a) gives

$$I(0; \mu) = \mathcal{B}_o e^{-\tau^*/\mu} + \mathcal{B}_o[1 - e^{-\tau^*/\mu}] = \mathcal{B}_o \tag{7.8}$$

Thus the intensity is uniform, regardless of the direction of observation (in this case it is said to be *isotropic*). This occurs because the portion of radiation emitted by the surface and absorbed by the atmosphere is precisely compensated by the emission from the atmosphere. Figure 7.3 presents a plot of each term of the right–hand side of (7.8) as a function of τ^* assuming a value of $\mathcal{B}_o = 1$. The second term represents the atmospheric emission and increases as τ^* increases. This characteristic increase is referred to as a curve of growth of I with respect to τ^* and is important to a number of emission–based remote sensing methods that are described later.

Figure 7.3 serves to illustrate two important elements of emission based sensing of the atmosphere. The first of these is that it is necessary to be able to distinguish between the atmospheric and surface contributions. Circumstances that provide a large contrast between the surface and atmosphere, such as occurs at microwave frequencies over water surfaces, allow us to isolate the atmospheric signature more or less unambiguously. The second aspect is that the key parameter in the emission sensing is the optical depth and

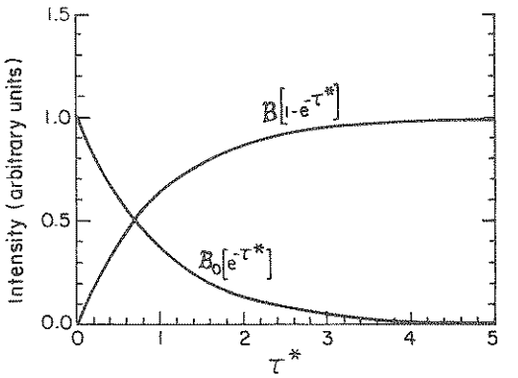

Figure 7.3 Contributions to the upwelling intensity at $\mu = 1$ at the top on an atmosphere of optical depth τ^* from the top of an isothermal atmosphere due to emission from the surface and emission from the atmosphere. The intensity is expressed in normalized units.

all methods that derive atmospheric properties from emission measurements establish a relationship between τ^* and the property of interest. Several examples of these relationships are discussed later.

For a nonisothermal atmosphere, solutions of either (7.6a) or (7.6b) are usually carried out using numerical integration methods. For illustrative purposes, however, the example of a Planck function that is a linear function of optical depth yields both simple and useful solutions to these equations[2]. Let $\mathcal{B}_o$ and $\mathcal{B}^*$ be the values of the Planck function at the top and bottom of the atmosphere, respectively. It follows from direct integration of (7.6a) and (7.6b) with $\mathcal{B}_o + (\mathcal{B}^* - \mathcal{B}_o)\tau/\tau^*$ substituted for $\mathcal{B}(\tau)$ that the upward looking instrument sees radiation that varies with μ according to

$$I(\tau^*; -\mu) = \mathcal{B}_o\left(1 - e^{-\tau^*/\mu}\right) + (\mathcal{B}^* - \mathcal{B}_o)\left[1 - \frac{\mu}{\tau^*}\left(1 - e^{-\tau^*/\mu}\right)\right] \tag{7.9}$$

which again predicts limb brightening. The downward looking instrument detects an angular variation in intensity of the form

[2] There is quite a subtle, but nevertheless important, point to recognize when the Planck function is approximated in this way. The radiative transfer equations described throughout this chapter apply to a single wavelength. A linear–in–τ Planck function implies that the variation of temperature with z varies unrealistically from one wavelength to another.

$$I(0;\mu) = \mathcal{B}^* e^{-\tau^*/\mu} + \mathcal{B}^* \left(1 - e^{-\tau^*/\mu}\right) -$$

$$(\mathcal{B}^* - \mathcal{B}_o)\left[1 - \frac{\mu}{\tau^*}\left(1 - e^{\tau^*/\mu}\right)\right] \qquad (7.10)$$

which is no longer isotropic but decreases as the instrument scans toward the horizon (*limb darkening*).

In general, we learn from these simple examples that the amount of limb darkening or brightening depends upon the vertical distribution of temperature (that is on both $\mathcal{B}^*$ and $\mathcal{B}_o$) and on τ^*. There is also generally less angular variation in the upwelling intensity than for the downwelling field, particularly at wavelengths where τ^* is small, because the atmosphere transmits some of the radiation incident upon it from the underlying surface. As the optical depth increases, the angular variation of the downward intensity decreases because most of the radiation originates nearer the detector. The upward intensity generally changes relatively slowly with angle, except in the limb.

7.2 The Remote Sensing of Sea Surface Temperature

Except for a few selected examples, most topics in this book deal with the remote sensing of atmospheric properties. There are many surface properties that influence the atmosphere in significant ways. It is also important for studies of the atmosphere to monitor these properties. Sea and land surface temperatures, for example, fundamentally impact upon both the weather and the climate of Earth. In fact, global monitoring of sea surface temperature (SST), in particular, looms as one of the most important exercises in the study of the Earth's climate and the potential for climate change. Some appreciation of the need for remote measurements of SST is provided in Fig. 7.4 which exemplifies the current distribution of in situ SST observations from ships and buoys. The density of observations is greatest in the oceans of the northern hemisphere, and data coverage is sparse over the southern hemisphere oceans. This situation is obviously inadequate for climate studies of SSTs and is clearly inadequate for monitoring global temperature.

The remote sensing of surface temperature is commonly done using measurements of the Earth–atmosphere emission at various wavelengths. The general idea is to measure the emission at wavelengths where the atmosphere is most transparent. Unfortunately,

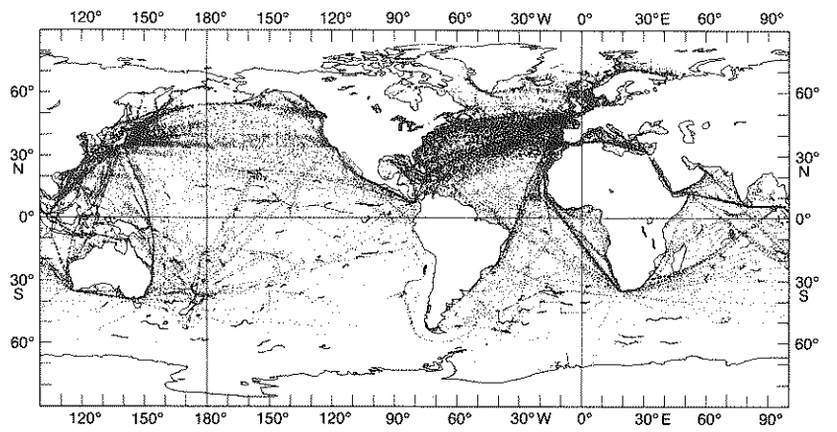

Figure 7.4 Distribution of surface marine in situ (ship and buoy) observations for October 1986. Drifting buoys are distinguished as nearly continuous wiggly lines (after Reynolds, 1988).

the atmosphere is never completely transparent in the main "windows" even for clear skies; therefore, some method is needed to correct for the atmospheric emission. A technique that attempts to provide such a correction is the "split–window" approach which uses measurements at multiple wavelengths. This multichannel approach (referred to as MCSST) originates from the spectral transfer equation, (7.6a), written in the form

$$I(\tau \approx 0, +\mu) = \mathcal{B}(T_s)\mathcal{T}(\tau^*, \mu) + \mathcal{B}(T_a)[1 - \mathcal{T}(\tau^*, \mu)] \qquad (7.11)$$

where the emission from the surface is approximated by the blackbody function $\mathcal{B}(T_s)$ at the surface temperature T_s. In (7.11), $\mathcal{T}(\tau^*, \mu) = e^{-\tau^*/\mu}$ is the transmittance of the atmosphere along the slant path defined by μ and extending from the surface to the satellite. We also express the emission by the atmosphere in terms of an effective blackbody temperature T_a defined from the relationship

$$\mathcal{B}(T_a) = [1 - \mathcal{T}(\tau^*, \mu)]^{-1} \int_0^{\tau^*} \mathcal{B}(t) e^{-t/\mu} \frac{dt}{\mu} \qquad (7.12)$$

The split–window technique uses observations at two channels in an attempt to eliminate the term containing T_a from (7.11) and solve for T_s. To explore this approach, suppose we measure the two

intensities at adjacent wavelengths λ_1 and λ_2. We represent these measurements by I_1 and I_2 and it follows from (7.11) that

$$I_1 = \mathcal{B}_1(T_s)\mathcal{T}_1(\tau_1^*, \mu) + \mathcal{B}_1(T_a)[1 - \mathcal{T}_1(\tau_1^*, \mu)] \tag{7.13a}$$

$$I_2 = \mathcal{B}_2(T_s)\mathcal{T}_2(\tau_2^*, \mu) + \mathcal{B}_2(T_a)[1 - \mathcal{T}_2(\tau_2^*, \mu)] \tag{7.13b}$$

Prabhakara et al. (1974) claim that the value of T_a varies by less than 1 K across the 10.5–12.5 μm window so it is also reasonable to assume a common value for T_a. It is also reasonable to expect that the surface emissivities are the same at adjacent wavelengths (here we conveniently assume this emissivity to be unity).

To solve for T_s, we make use of Taylor's theorem to arrive at the following

$$\mathcal{B}_\lambda(T) \approx \mathcal{B}_\lambda(T_a) + \frac{\partial \mathcal{B}_\lambda}{\partial T}(T - T_a)$$

where the partial derivative is evaluated at $T = T_a$. Application of this equation to both wavelengths and further elimination of the $T - T_a$ factor yields

$$\mathcal{B}_2(T) \approx \mathcal{B}_2(T_a) + \frac{\partial \mathcal{B}_2/\partial T}{\partial \mathcal{B}_1/\partial T}[\mathcal{B}_1(T) - \mathcal{B}_1(T_a)] \tag{7.15}$$

We use this expression twice, once to approximate our observation I_2, which we write in terms of a brightness temperature $T_{b,2}$ according to $I_2 = \mathcal{B}_2(T_{b,2})$, and a second time to approximate $\mathcal{B}_2(T_s)$ to obtain

$$\mathcal{B}_1(T_{b,2}) = \mathcal{B}_1(T_s)\mathcal{T}_2 + \mathcal{B}_1(T_a)[1 - \mathcal{T}_2] \tag{7.16}$$

Eliminating $\mathcal{B}_1(T_a)$ from (7.13a) and (7.16) yields the split–window equation

$$\mathcal{B}_1(T_s) = I_1 + \eta[I_1 - \mathcal{B}_1(T_{b,2})] \tag{7.17}$$

where

$$\eta = \frac{1 - \mathcal{T}_1}{\mathcal{T}_1 - \mathcal{T}_2} \tag{7.18}$$

This relationship is further approximated and linearized in terms of the brightness temperatures,

$$T_s \approx T_{b,1} + \eta[T_{b,1} - T_{b,2}] \tag{7.19}$$

In practice, the actual split–window technique is rarely used in the form given by either (7.17) or (7.19) but these serve merely as a justification for regressing the surface temperature as a linear function

of the measured brightness temperatures. The more typical form of this regression is

$$SST = aT_{11} + b(T_{11} - T_{12}) - c \tag{7.20}$$

where the coefficients a, b, and c are empirically derived from in situ observations such as obtained from drifting buoys. In this expression, $T_{11,12}$ are the brightness temperatures of the $11\mu m$ and $12\mu m$ channels of the AVHRR instrument. When comparing the satellite observations to conventional observations, it is important to note that the satellite temperatures correspond to the temperature of a surface layer just a few millimeters thick (this is referred to as the "skin" temperature). In situ measurements, on the other hand, are bulk measurements of the temperature of a layer of water perhaps a few meters deep. The regression approach of the MCSST is an attempt, in part, to tune the satellite skin temperatures to the in situ bulk temperature. Part of this tuning also accounts for the fact that the atmosphere is not completely transparent at the window wavelengths, especially over the moist tropics (discussion of Table 3.1 and Problem 7.6 offer more quantitative perspectives of these atmospheric effects).

The multichannel approach described here is presently used operationally by NOAA; the precise details of the operational algorithm are described by McClain et al. (1985). The approach actually uses both the $11\mu m$ and $12\mu m$ channels of the AVHRR and the $3.7\mu m$ window channel and has a form similar to that of (7.20). An important part of the algorithm, and one of relevance to many retrieval problems involving infrared emission measurements, is the need to establish whether or not clouds appear in the field of view. Undetected clouds are a source of bias when temperatures associated with the emission from clouds are mistakenly mixed with the SSTs.

Another problem associated with the MCSST approach is that the retrieval of SST is affected by other changes in the atmospheric infrared opacity that occur, for example, with increased concentrations of stratospheric aerosol from volcanic eruptions. Figure 7.5 shows a monthly time series of in situ and satellite observations for the 1982–1986 period for two eastern Pacific regions: one in the tropics (labeled Nino–3) and one in the northern midlatitudes (Namais). The satellite–derived SSTs are lower overall than are the in situ values by about 0.5 degrees; however, the bias is approximately 2 degrees during the period of the El Chichon eruption.

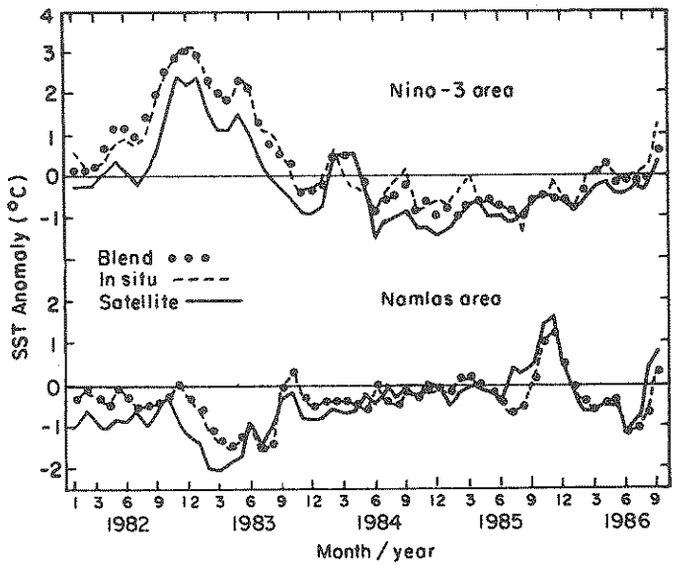

Figure 7.5 Time series of in situ (dashed) and satellite (solid line) SST anomalies for the period shown. The blended data are given as dotted curves. The tropical Pacific region is referred to as Nino–3 and the midlatitude region is referred to as Namais (after Reynolds, 1988).

Reynolds (1988) describes a method which attempts to blend the SST observations from ships and buoys with the satellite observations in an attempt to remove biases of this type. The philosophy is to use the in situ observations as a kind of "benchmark" and the satellite observations are used to define the shape of fields in regions where there is little in situ data. This approach attempts to overcome these biases and is used to develop a climatological SST data set. An example of the comparison of the blended product to the in situ and satellite data is also shown in Fig. 7.5 for the two east Pacific regions.

7.3 Examples of Path–Integrated Quantities

The microwave radiation emitted from the surface of the Earth and sensed by an instrument on a satellite is modulated by processes of emission, absorption, and scattering in the atmosphere; thus, it depends upon the properties of the Earth's surface, atmospheric constituents, and hydrometeors (water droplets, rainfall and ice crystals). The microwave emission from the surface of the Earth depends both on the physical temperature and the emissivity of the surface. Over oceans, values of emissivity typically vary between 0.4 to 0.5, and the emissivity depends on the surface wind speed (refer to Section 4.5). Thus the emission from the ocean is relatively constant and provides a low–level background signal for observing atmospheric emission. Over land, however, both temperature and emissivity are highly variable. The temperature of the land varies with solar insolation, both diurnally and in response to clouds. Land temperature is also a function of the surface albedo, evaporation and evapotranspiration, wind speed, and other factors. The land–surface emissivity is dependent on the thickness, type, and water content of the vegetation canopy and the moisture content and type of the soil. This makes the microwave background signal over land highly variable and measurements subsequently more difficult to interpret. Because of this difficulty, the methods now described are applied only over oceans or over large water bodies on land.

A method that provides vertically integrated water vapor (we refer to this as the *precipitable water*) and the vertically integrated cloud liquid water amount is now described. This method makes use of measurements of the microwave emission by the atmosphere and Fig. 7.6 offers a physical perspective on the approach. Shown are theoretically derived brightness temperature spectra from 6.6 to 37 GHz calculated by a radiative transfer model assuming conditions relevant to a tropical atmosphere. The solid, almost straight, line is the brightness temperature that would be measured over the ocean in the absence of any atmospheric absorption. A calm ocean surface therefore appears cold and the overlying atmosphere appears warm against this cold background due to the increased emission by water vapor and liquid water. The amount of warming is related to the amount of increased emission by the atmosphere associated with the amount of water vapor and liquid water distributed along the path. The solid curve indicates the absorption line centered at 22.235 GHz and is derived for a water vapor overburden of 34.2 kgm^{-2}. The dashed curve is the spectrum produced when a cloud layer containing 0.5 kgm^{-2} of liquid water droplets (a value perhaps typical of low–level stratiform clouds) is added to the atmosphere. Cloud droplets at these wavelengths are assumed to be Rayleigh particles (Section 5.3) and produce a systematic increase in emission at all frequencies over and above that due to water vapor. The dif-

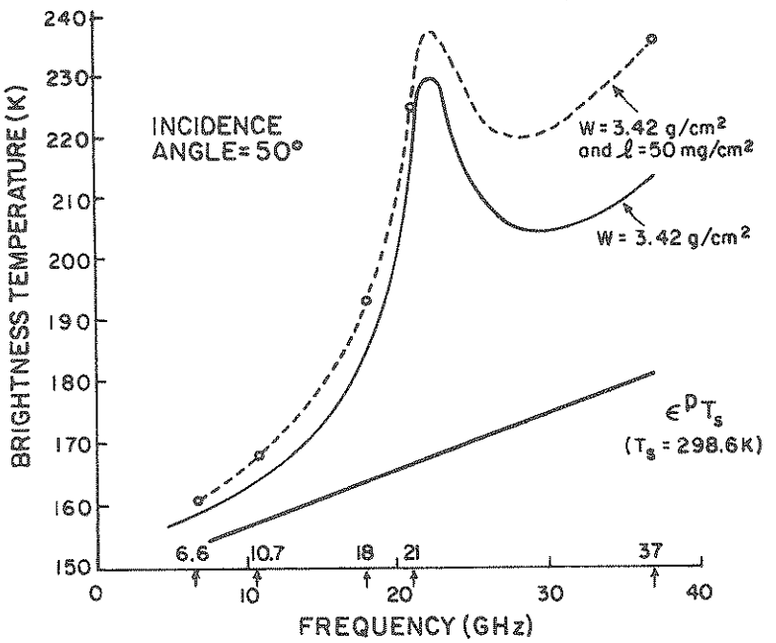

Figure 7.6 Brightness temperature spectra between 6 and 37 GHz for no atmosphere (solid line), a tropical model atmosphere with 34.2 kgm^{-2} of precipitable water (solid curve), and the addition of 0.5 kgm^{-2} of cloud liquid water (from Prabhakara et al., 1982).

ference in brightness temperature associated with the emission by cloud droplets and water vapor increases as the spectral frequency increases. Also shown for reference are the spectral positions of the channels of two satellite microwave radiometers, the Scanning Multichannel Microwave Radiometer (SMMR) flown on the experimental Nimbus 7 satellite (upward pointing arrows) and the Special Sensor Microwave Imager (SSM/I – downward pointing arrows) which has been used operationally since July 1987 as part of the Defense Military Satellite Program.

7.3.1 Microwave Radiative Transfer

It is important to realize that a significant portion of the microwave intensity emitted from the atmosphere toward the ocean surface is reflected back to the atmosphere. Furthermore, the emissivity is polarized by an amount dependent on the viewing direction (Section

4.5). Equation (7.6a) can be readily modified to account for these factors in the following way,

$$T_B = \epsilon^p T_s e^{\tau^*/\mu} + \int_0^{\tau^*} T(t) e^{-(t-\tau)/\mu} d(\frac{t}{\mu})$$

$$+\mathcal{R}^p e^{-\tau^*/\mu} \int_{\tau^*}^{0} T(t) e^{-(\tau^*-t)/\mu} d(\frac{t}{\mu}) \qquad (7.21)$$

where T_B is the brightness temperature measured at the satellite altitude,[3] T_s is the sea surface temperature, ϵ^p is the emissivity of the ocean surface with the given polarization state p, and $\mathcal{R}^p = (1 - \epsilon^p)$ is the surface reflectivity. The first term of the right–hand side of (7.21) is the surface emission term, the second defines the integrated atmosphere emission, and the third corresponds to the downwelling radiation emitted by the atmosphere, reflected at the surface and then transmitted to the satellite sensor. A simplification to (7.21) can be made if it is assumed that the absorption by water vapor is confined to the boundary layer. Thus

$$\int_0^{\tau^*} T e^{-(t-\tau)/\mu} d(\frac{t}{\mu}) \approx T_s \int_0^{\tau^*} e^{-(t-\tau)/\mu} d(\frac{t}{\mu}) \approx T_s \left(1 - e^{-\tau^*/\mu}\right) \qquad (7.22)$$

where we have specifically assumed that the emitting temperature of the water vapor is the same as the sea surface temperature. Refinements to this approximation to include vertical variations of temperature are relatively simple to make but lead only to relatively small corrections to what is presented below so these are omitted here. On substitution of (7.22) into (7.21) we obtain

$$T_B \approx T_s \left[1 - \mathcal{T}^2(\mu)(1 - \epsilon^p)\right] \qquad (7.23)$$

where $\mathcal{T}(\mu) = e^{-\tau^*/\mu}$ is the transmissivity along the direction defined by μ.

[3] We can invoke the Rayleigh–Jeans distribution for $\mathcal{B}$ for many of the microwave frequencies of interest in this book and thus replace this function simply by the temperature T (refer to the discussion in Section 2.5 for more details).

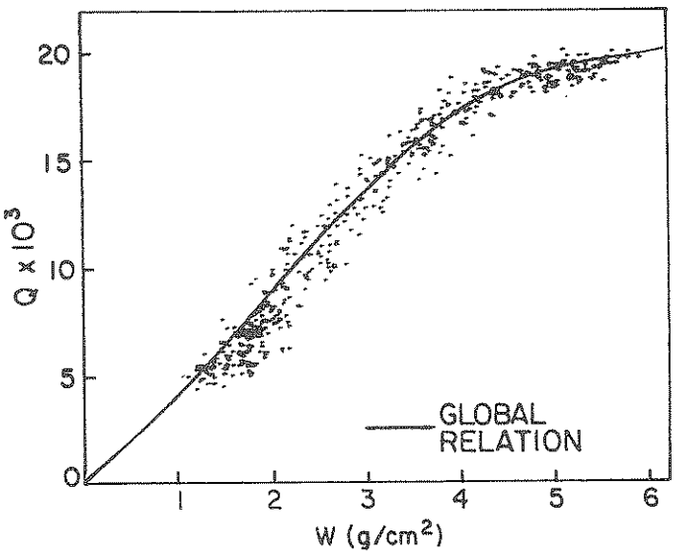

Figure 7.7 Scatter plot of sea–level water vapor mixing ratio and precipitable water for July data in the northern hemisphere and for January data in the southern hemisphere (Liu, 1986).

Excursus: Surface–Level Humidity and Heat Fluxes Over the Ocean

Atmospheric scientists have long been interested in the relationship between vertically integrated path quantities, like precipitable water, and surface observations of properties such as the dew–point temperature, mixing ratio, and vapor pressure. Over the past few years, the association between precipitable water derived from microwave emission measurements and surface level mixing ratio has been studied. A relationship between these quantities is particularly important over the ocean regions where observations are lacking and where this information is crucial for studies of air–sea interaction.

Using 17 years of sounding data from 49 ocean stations, Liu (1986) proposes an empirical relationship between mixing ratio near the surface and precipitable water, an example of which is shown in Fig. 7.7. This relationship provides us with a way of estimating the flux of water vapor E via the bulk parameterization

$$E = \rho_{air} C_E v (q_s - q)$$

where ρ_{air} is the density of surface air, C_E is a specified transfer coefficient, q_s is the saturation humidity at the surface, v is the near–surface wind speed and q is the humidity of air at some level just above the surface (usually within the surface layer such that v and q are observed at the same height). This value of q is determined from satellite observations of precipitable water using the a priori relationship between q and w. The latent heat flux then follows as the product of E and the latent heat of vaporization L. In principle, the wind speed at the surface can also be estimated from spaceborne sensors using methods like those described earlier. It is therefore possible to estimate E and LE from satellite observations provided we know C_E and ρ_{air}. Liu and Niiler (1984) propose this approach for estimating the monthly mean latent heat fluxes and claim an accuracy of approximately 20 Wm^{-2} for these fluxes.

7.3.2 A Microwave Method for Integrated Water Vapor and Cloud Water

Both the vertically integrated water vapor and cloud liquid water contents are important quantities in the study of the Earth's climate system and especially relevant to topical problems of global change. Figure 7.6 also illustrates how the emission of microwave radiation arises from emission by vapor and by cloud liquid water droplets. This emission is unpolarized whereas the microwave radiation from the ocean surface is polarized to some degree (as described in Section 4.5). The stronger the absorption and thus the stronger the emission by the atmosphere, the more obscured is this polarization. A scheme that exploits this property of emission to derive vertically integrated water vapor and cloud liquid water contents will now be described. The method begins with the approximation (7.23) to analyze the 19.35 GHz and 37 GHz brightness temperatures for the two measured polarization states. This equation is differenced relative to these two polarizations to produce

$$\Delta T_B = T_s \left(\mathcal{R}^V - \mathcal{R}^H \right) \mathcal{T}^2 \tag{7.24}$$

at each frequency where $\mathcal{R}^{V,H} = 1 - \epsilon^{V,H}$ represents the surface reflectivity in the horizontal (H) and vertical (V) polarization states. These surface reflectivities are functions of wind speed as we have previously described. The square of the atmospheric transmission is

$$\mathcal{T}^2 = \mathcal{T}_w^2 \mathcal{T}_W^2 \mathcal{T}_{ox}^2$$

which includes the transmission factor for O_2 and factors for cloud liquid water $\mathcal{T}_W = \exp(-k_\ell W/\mu)$ and water vapor $\mathcal{T}_w =$

$\exp(-k_w w/\mu)$ where k_ℓ is the absorption coefficient of liquid water (the form of this coefficient is described in Section 5.3) and k_w is the absorption coefficient for vapor. With some rearrangement of (7.24), it follows that

$$k_\ell W + k_w w = -\frac{\mu}{2} \ln \frac{\Delta T_B}{T_s(\mathcal{R}^V - \mathcal{R}^H)\mathcal{T}_{ox}^2} \tag{7.25}$$

This equation, applied to both the 19 GHz and 37 GHz measurements, constitutes a set of linear simultaneous equations which can be solved for w and W given values of $\mathcal{T}_{ox,19}$, $\mathcal{T}_{ox,37}$, Δk_w, and Δk_W and modeled values of $\mathcal{R}^V$ and $\mathcal{R}^H$. These surface reflectivities are functions of wind speed as previously noted in Chapter 4.

Knowing just what values to use for the absorption coefficients is perhaps the greatest source of uncertainty not only to the retrieval described here but also to most retrievals of water vapor based on measurements of atmospheric emission. Values of k_ℓ can be taken from a number of sources and the values of k_W in principle follow from the particle scattering theories discussed in Chapter 5. The temperature dependence of k_W arising from the temperature dependence of the refractive index of water at these microwave frequencies is yet another source of uncertainty.

Examples of the precipitable water w derived from this retrieval method are given in Figs. 7.8a and b as four–year seasonal averages of w for December–January–February and June–July–August, respectively. The uncertainty in w is estimated to be about 3 kgm^{-2} based on comparisons with near coincident radiosonde data. The distribution of monthly mean w broadly follows the distribution of SST (Stephens, 1990) with the largest amount over the warmest waters of the equatorial western Pacific Ocean.

One significant factor that has limited the wide use of microwave liquid water data is the general lack of independent data to verify retrievals. Greenwald et al. (1992) attempt such a verification using a limited amount of independent ground–based microwave measurements of W as well as an estimate derived from AVHRR measurements of reflected sunlight. Comparisons between near coincident SSM/I satellite values of W with those of both AVHRR and the surface microwave measurements are presented in the form of a scatter plot in Figs. 7.9a and b, respectively, for stratocumulus clouds off the west coast of California. The error bars are meant to signify the extent of spatial variability associated with the measurements and represent one standard deviation above and below the mean value.

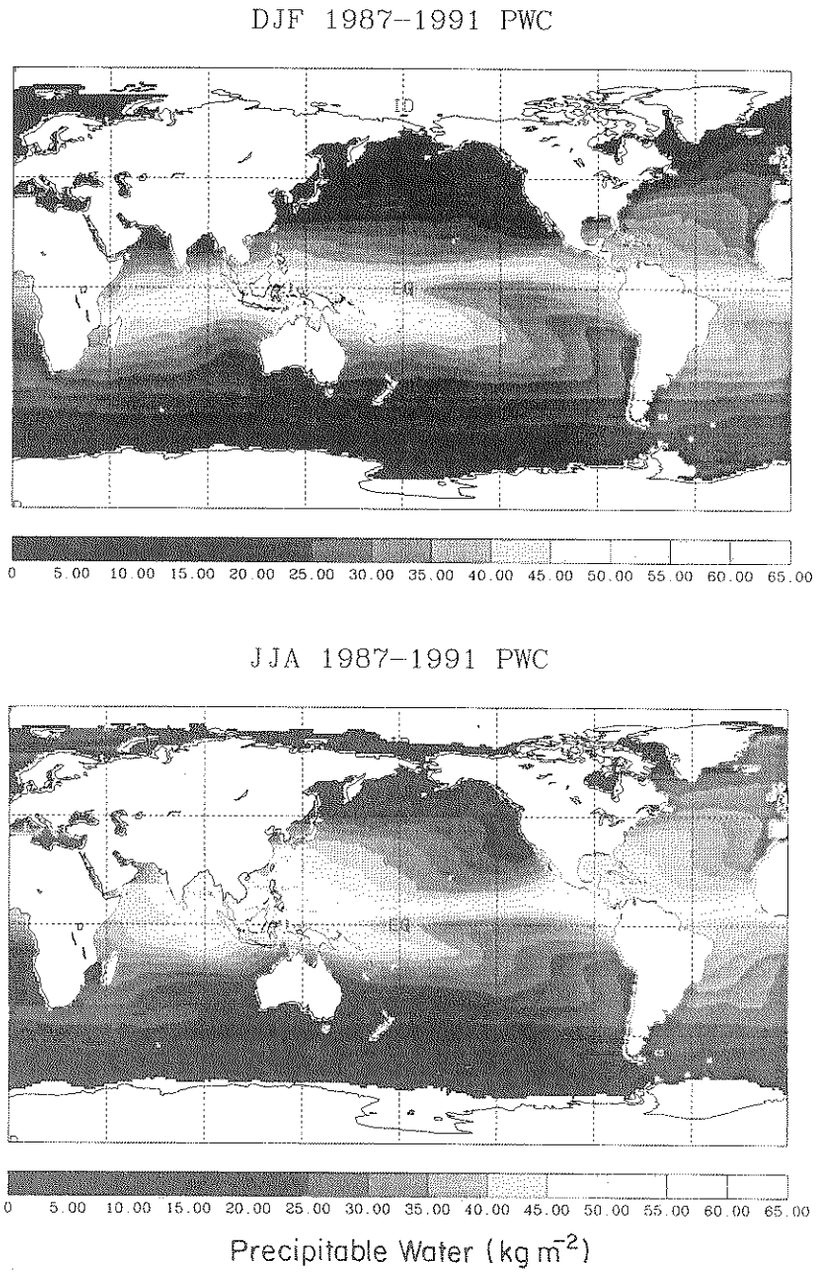

Figure 7.8 (a) The DJF averaged precipitable water derived as an average of DJFs from four years of data. (b) Same as (a) but for the JJA season (Jackson and Stephens, 1993).

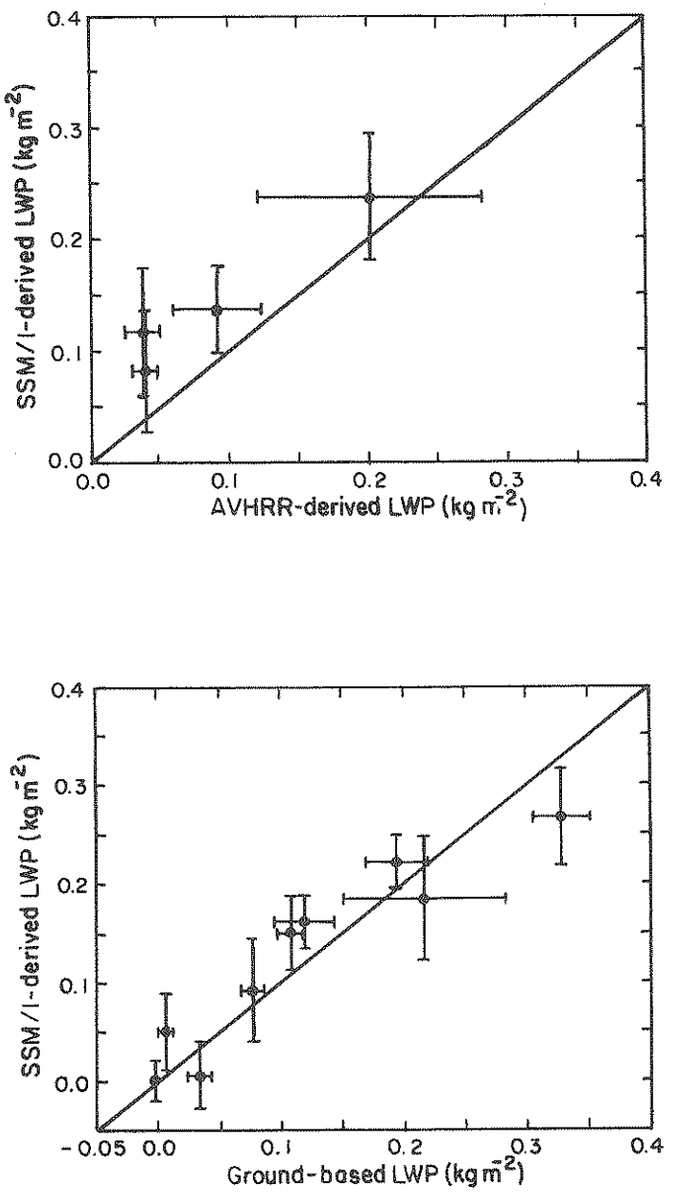

Figure 7.9 Scatter plot of W derived from the microwave retrieval method based on SSM/I measurements with those derived from AVHRR (a) and surface microwave measurements (b). The horizontal and vertical lines about each point are meant to convey the extent of variability in the measurements (Greenwald et al., 1993).

It is yet to be shown if this level of agreement is reasonable and these comparisons do not constitute a rigorous test of the approach, especially when applied to provide global distributions of W. With this in mind, the distribution of W derived from emission measurements over oceans are shown in Fig. 7.10 for August 1987 and February 1988. The main characteristics of global cloudiness are reproduced in these maps including the predominant regions of cloudiness associated with the Inter–Tropical Convergence Zone (ITCZ), the South Pacific Convergence Zone (SPCZ) and the cloudiness associated with midlatitude storminess.

7.4 Passive Sensing of Rainfall

Precipitation, in the form of rainfall, is a key component of the Earth's hydrological cycle. The need to obtain better observations of precipitation globally as well as the need to incorporate more realistic cloud processes in models of the large scale atmospheric motion has prompted more interest in the possibility of space–borne observations of precipitation.

A number of methods exist for the remote sensing of rainfall. Two of these, based on radiation emitted by clouds and rainfall, will now be described and Fig. 7.11 provides a convenient framework for contrasting these two techniques. The diagram presents measurements of radiation at a number of frequencies as a function of elapsed time along a flight path of an instrumented aircraft. The emissions at 18, 37, 92, and 183 GHz are presented in terms of brightness temperature as is the emission at 11 μm. The bottom shaded portion of each panel is the rainfall rate deduced by radar (methods for estimating rainfall from radar measurements are described in Chapter 8). As the aircraft overflies the cloud system, the 11μm brightness temperature decreases from about 245 to 205 K. This decrease occurs at the edge of the deepening outflow anvil from the thunderstorm complex. The microwave temperatures do not show a corresponding drop indicating that the cloud is transparent at these frequencies and presumably composed of ice crystals much smaller than the wavelength of the radiation in question. Passage of the aircraft across the coastline from ocean to land is indicated by an increase in the microwave brightness temperatures due to the sharp rise in surface emissivity at these frequencies. Over the area of deep convection and heavy rain, small decreases (10 to 15 K) in the 11μm brightness temperatures associated with overshooting cells are ob-

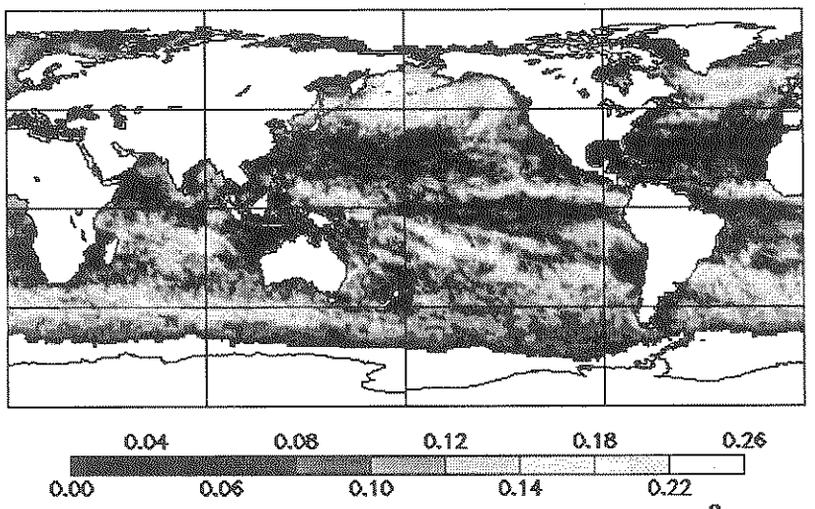

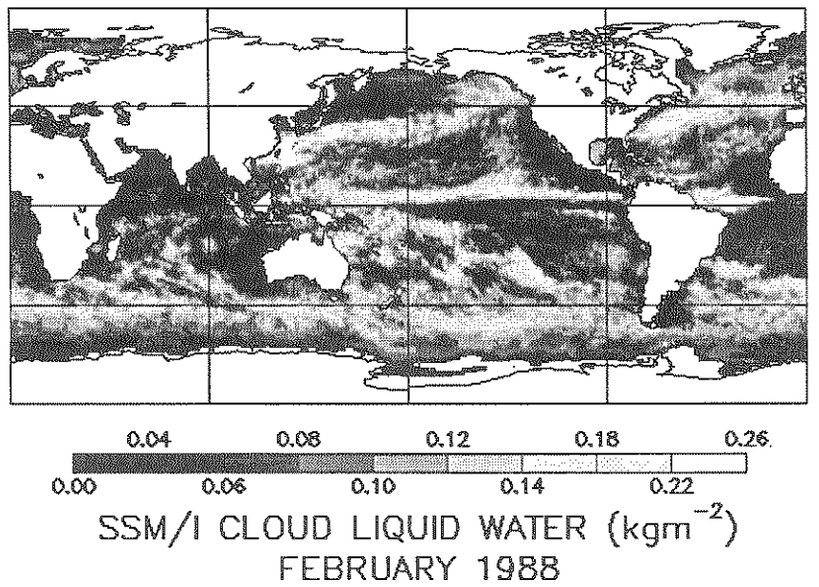

Figure 7.10 Global distributions of cloud liquid water derived from SSM/I observations for August 1987 (top) and February 1988 (bottom) (Greenwald et al., 1993).

served, but the correlation between the decreased emission in these regions and precipitation as indicated by radar measurements is obviously weak. A deep layer of cloud composed of relatively large ice particles leads to significant depressions in the measured microwave temperatures over these deep cores. Values of this depression are as large as 70 to 100 K for the higher frequency 92 and 183 GHz channels due to scattering of radiation at these frequencies by large ice particles. Although this scattering increases with increasing frequency, its effect is even apparent in the 18 and 37 GHz channels. The minima in the 18 GHz time series broadly correspond to the peaks in convective rainfall (these are denoted by the letters A, D, E, and G). It is this general relationship between microwave brightness temperature and rainfall that serves as the basis for microwave sensing of precipitation. These results, however, demonstrate how ice particle scattering complicates microwave emission estimates of rainfall especially for frequencies greater than about 37 GHz.

7.4.1 Rainfall Estimates from Outgoing Longwave Radiation (OLR)

Satellite infrared image data have been used extensively over the past two decades in an attempt to derive rainfall. The basic idea of this approach assumes that the rainfall rate is related in some way to the depth of the cloud and thus to cloud top temperature. Since measurements of the IR emission at window wavelengths provide a way of estimating this temperature, the OLR is assumed to be related to rainfall. Estimates of the outgoing longwave radiation have been available since 1974 from the window channel measurements available from operational NOAA polar–orbiting satellites. It was quickly realized that OLR provides a qualitative index of tropical convection and over large, fixed areas in excess of 10^4 km^2 the OLR is found to be significantly correlated to rainfall. Arkin (1979) and Richards and Arkin (1981) estimate that 50 to 70% of the variance of areally averaged rainfall accumulations measured during the GARP Atlantic Tropical Experiment (GATE) is explained by a linear function of the mean fraction of the area covered by cloud with equivalent black body temperatures colder than thresholds ranging between 220 and 250 K. Largest values of explained variance were found for a brightness temperature threshold of 235 K and for areal averages defined by a grid 2.5 degrees latitude/longitude on a side. These gross statistical correlations suggest that OLR precipitation

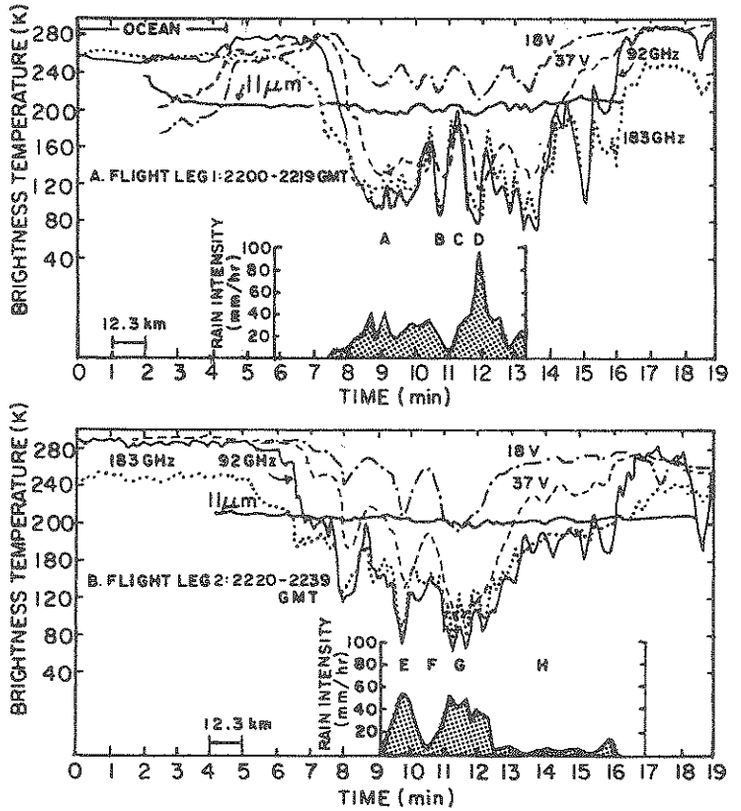

Figure 7.11 Observed brightness temperatures at 11 μm, 18 and 37 GHz, and at 92 and 181 GHz as a function of NASA's ER-2 flight path for two different time segments. Also shown is the low-level radar-based rain rate for the portion of the flight path where radar data are available (Adler et al., 1990).

estimates may play some useful role in climatological studies of precipitation

Arkin and Meisner (1987) applied this threshold method to IR imagery from the GOES satellite to arrive at a rainfall estimate according to

$$\mathrm{GPI} = 3A_c t$$

where GPI is the rainfall estimate referred to as the GOES Precipitation Index and is expressed in millimeters, A_c is the fractional area (dimensionless between 0 and 1) of cloud colder than 235 K in a $2.5^o \times 2.5^o$ box, and t is the length of the period (hours) for which A_c was the mean fractional cloudiness. The product of A_c with duration t is referred to as the area-time-integral (ATI) and we will return to this product quantity in Chapter 8.

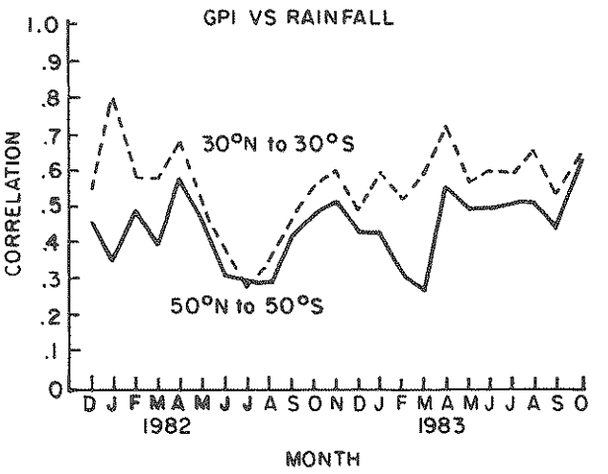

Figure 7.12 Time series of the spatial correlation between monthly rainfall observed at 465 stations and the GPI for the entire 30°N to 30°S region and for the entire 50°N to 50°S region (Arkin and Meisner, 1987).

Figure 7.12 presents the correlation of the GPI with independent station measurements of precipitation for the region extending from 30°N to 30°S and from 50°N to 50°S. The station data used in this comparison were limited to only 465 stations which is only a very small percentage of the study area. The secular variation in the correlation for the two regions demonstrates that OLR and rainfall are more highly correlated in the tropics throughout the period of study possibly because of the higher frequency of convective rainfall in that region.

This analysis serves to illustrate one of the main problems with present satellite rainfall retrieval methods. There is a general lack of extensive ground truth observations for verification. This is also an inherent problem for the remote sensing of SST over southern oceans and for the retrieval of cloud liquid water, although it is perhaps even more severe for precipitation due to the inherent small-scale spatial variability of rainfall. Despite this problem, efforts are underway to produce more global distributions of rainfall deduced from satellite measurements. Figure 7.13 is an example of such an attempt and shows maps of the GPI over the tropics. The regions not covered by the GOES were filled in using NOAA polar orbiting satellite data to produce these maps. The anticipated characteristics of tropical precipitation seem to be well reproduced in this analysis,

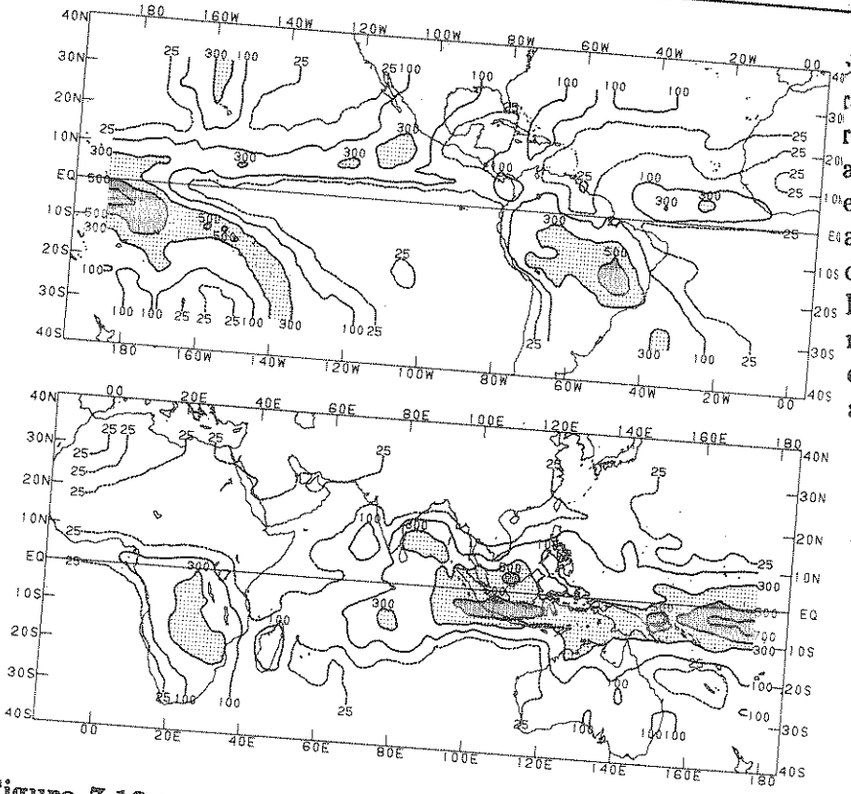

Figure 7.13 Estimated rainfall (millimeters), on a 2.5°× 2.5° grid for the period December 2–31. Areas of missing geostationary satellite data have been filled in using OLR data from the NOAA polar–orbiting satellite (Arkin and Ardanuy, 1989).

including heavy precipitation in areas of deep convection located over the Indonesian maritime continent, the Amazon and Congo basins as well as the precipitation associated with the ITCZ and the SPCZ.

7.4.2 Microwave Emission Methods for Sensing Rainfall

Although retrieval of rainfall from microwave emission measurements suffers from its own ambiguities, as highlighted in Fig. 7.11, these measurements in principle offer a more direct way of estimating rainfall than do OLR measurements. The microwave technique exploits the direct consequences of the interaction between microwave radiation and precipitation–sized hydrometeors. This interaction is characterized by the optical depth τ^* associated with the emitting rain drops and the basis for estimating rainfall lies in an assumed relationship between this optical depth and the rainfall rate and a suitable contrast between the emission from the surface and the emission from the raindrops. Emission from raindrops, when viewed against a cold ocean background, increases with increasing optical depth in a manner illustrated by the curve of growth highlighted in Fig. 7.3. This increased emission, measured as an increased brightness temperature, is then associated with the rain rate $\Re$. We can explore a specific example of the relationship between $\Re$ and τ^* by assuming a Marshall–Palmer size distribution

$$n(D) = N_o e^{-\Lambda D} \tag{7.26}$$

where $N_o = 0.16$ cm^{-4} and

$$\Lambda = 81.56\Re^{-0.21} \tag{7.27}$$

where the rain rate $\Re$ is expressed in units of millimeters per hour. It therefore follows by definition that the volume extinction coefficient is

$$\sigma_{ext} = \frac{N_o}{4}\int_0^\infty n(D)\pi D^2 Q_{ext} dD. \tag{7.28}$$

Figure 7.14 presents calculations of σ_{ext} as a function of rain rate assuming the dielectric constant for water at $\lambda = 1.55$ cm (19.3 GHz) and $T = 273$ K. The calculations are based on the Lorenz–Mie theory and present both the extinction and scattering coefficients. These results show how the extinction is defined by the rain rate (under the assumption of the Marshall–Palmer distribution) and furthermore how the extinction at this frequency is largely governed by absorption processes since the scattering coefficient is almost an order of magnitude smaller than the absorption coefficient.

It is straightforward in principle to derive the brightness temperature associated with upwelling radiation as a function of τ^* and thus as a function of $\Re$. Figures 7.15a and b show examples of these relationships from synthetic data using output from a numerical cloud model as input into a numerical radiative transfer model. Each point is the microwave brightness temperature representative of a single square grid point of the model which is approximately 1.5 km on its side. The calculated brightness temperature is presented as a function of the modeled rain rate. The scatter diagram of Fig.

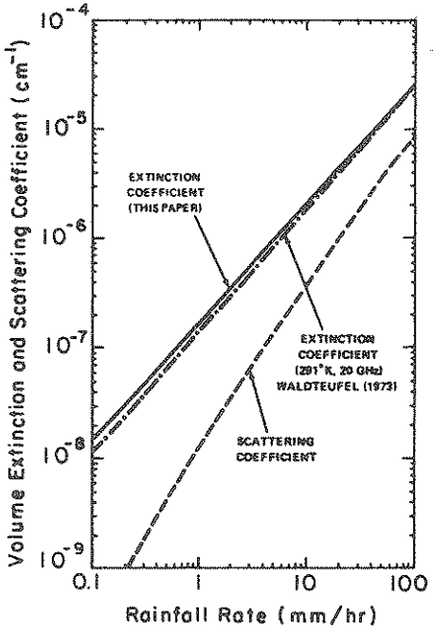

Figure 7.14 The volume scattering coefficient and volume extinction coefficient at $\lambda = 1.55$ cm for a Marshall–Palmer distribution of raindrops as a function of rain rate. The dielectric constant used in the calculations applies to water at T=273K (after Wilheit et al., 1977).

7.15a corresponding to 10 GHz exhibits the type of curve of growth expected from our simple model results graphed in Fig. 7.3. However, the equivalent relationship for 19 GHz is more complex for a number of reasons. In this case, scattering by the large ice crystals over regions of heaviest rainfall confuses matters. Radiation emitted from the underlying rain is scattered downward by the overlying layer of ice particles and away from any instrument looking downward above the cloud. This increase in scattering as $\Re$ increases leads to a decrease in brightness temperature.

Real data exhibit even more scatter than shown in Fig. 7.15b due to the highly variable spatial distribution of rainfall within an instrument field of view (this is referred to as the problem of *beam filling*). This is not treated in the results of Fig. 7.15 since the brightness temperatures are based on radiative transfer calculations that assume the rainfall to be horizontally homogeneous. Estimating rainfall from microwave emission measurements and understanding how the factors mentioned here, and others, affect these estimates remain topics of active research.

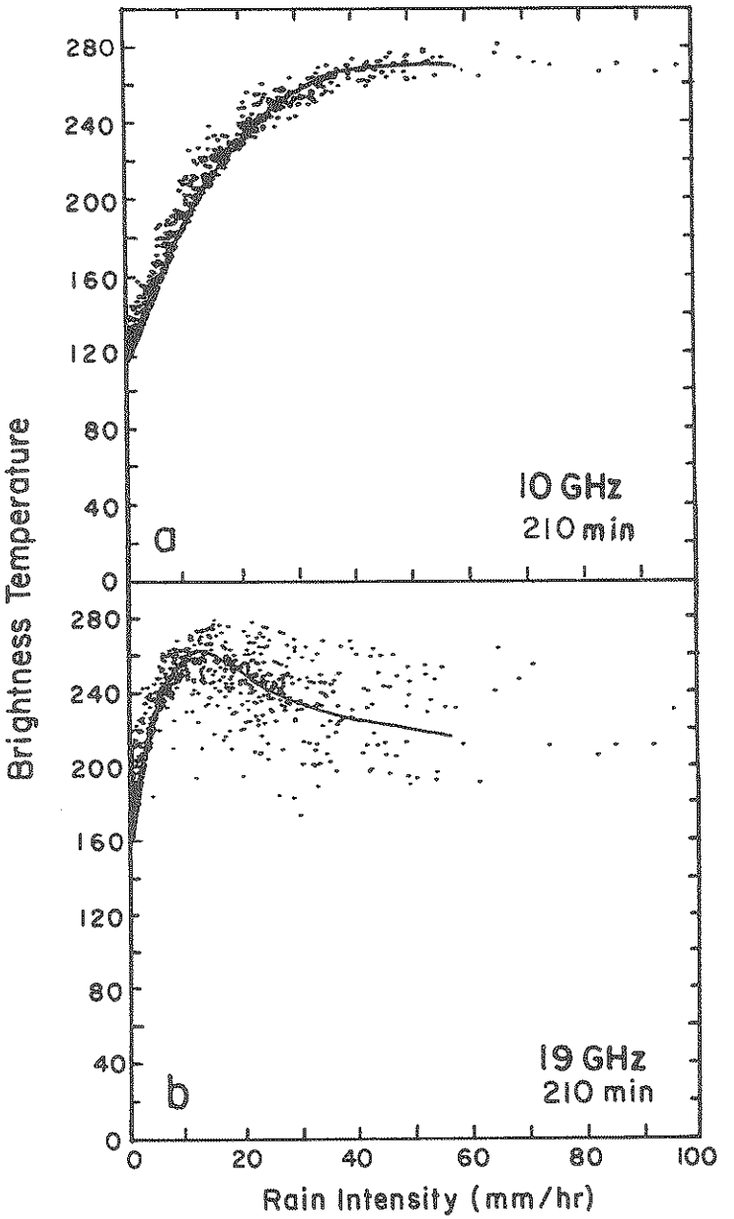

Figure 7.15 Scatterplots of microwave brightness temperature at 10 GHz (upper) and 19 GHz (lower) as a function of rain rate. The time indicated represents time into a cloud model simulation (from Adler et al., 1991).

7.5 Principles of Sounding by Emission

An important application of the particular type of radiative transfer discussed in this chapter centers on the inversion of the radiative transfer equation to retrieve vertical distributions of temperature and trace gas concentrations. The general basis of this inversion was outlined in the introductory chapter and much more can be found in the literature cited at the back of this chapter. This section intends only to provide the reader with a broad understanding of the physical basis for temperature sounding.

The basic approach of emission sounding of temperature is to detect the radiation emitted by gases of known distribution, like that of the uniformly mixed gases and specifically by the carbon dioxide molecule at wavelengths centered at 15 μm and by the oxygen molecule at frequencies around 60 GHz.

In discussing how temperature is retrieved from spectral intensity measurements, consider the following two experiments. The first setup has a radiometer at the ground and the second has a radiometer on a satellite that orbits the Earth. It is convenient to introduce

$$\mathcal{T}(t,\tau,\mu) = e^{-(t-\tau)/\mu} \tag{7.29}$$

as the transmittance along the path from the optical depth t to the optical depth τ along the direction defined by μ which we take to be the cosine of the zenith angle of observation. Therefore,

$$\frac{d\mathcal{T}}{dt}(t,\tau,\mu) = -\frac{1}{\mu}e^{-(t-\tau)/\mu} \tag{7.30}$$

and, on substitution into (7.6a), we obtain

$$I(\tau,\mu) = I(\tau^*,\mu)\mathcal{T}(\tau^*,\tau,\mu) + \int_{\tau^*}^{\tau} \mathcal{B}(t)\frac{d\mathcal{T}}{dt}(t,\tau,\mu)dt \tag{7.31}$$

The following notation

$$\mathcal{W}(\tilde{z}_1,\tilde{z}_2) = \frac{d\mathcal{T}}{d\tilde{z}}(\tilde{z}_1,\tilde{z}_2)$$

is used to refer to the quantity known as the *weighting function* for the reasons that become apparent later. In this definition, $\tilde{z}$ is taken to be an arbitrary vertical coordinate system such as altitude z, optical depth τ as in the case of (7.31), pressure p or $\ln p$. Therefore,

the weighting function is defined at some level $\tilde{z}_1$ relative to the measurement level $\tilde{z}_2$. In terms of this general vertical coordinate, (7.31) becomes

$$I(\tilde{z},\mu) = I(\tilde{z}^*,\mu)\mathcal{T}(\tilde{z}^*,\tilde{z},\mu) + \int_{\tilde{z}^*}^{\tilde{z}} \mathcal{B}(\tilde{z}')\mathcal{W}(\tilde{z}',\tilde{z},\mu)d\tilde{z}' \tag{7.32}$$

from which the meaning of the weighting function $\mathcal{W}$ emerges. Within the context of (7.32), the contribution to the intensity measured by a radiometer located at $\tilde{z}$ due to the emission from the layer $\Delta\tilde{z}'$ centered at $\tilde{z}'$ is determined from the local layer black body emission $\mathcal{B}(\tilde{z}')$ *weighted* by the factor $\mathcal{W}(\tilde{z}',\tilde{z})\Delta\tilde{z}'$. The functional form of $\mathcal{W}$ is of fundamental importance to vertical sounding problems and simple models are now described in an attempt to build an understanding of the general properties of $\mathcal{W}$ and how it depends on the strength and distribution of absorber.

7.5.1 Weighting Functions for Nadir Sounding

Absorption by molecules in the atmosphere below 50 km is strongly influenced by the collision broadening processes expressed in terms of the Lorentz line shape (refer to Chapter 3),

$$k_\nu = \frac{S\tilde{p}\alpha_{Lo}/\pi}{(\nu-\nu_o)^2 + \alpha_{Lo}^2\tilde{p}^2} \tag{7.33}$$

where α_{Lo} is the line width defined at a pressure $p_o = 1$ atmosphere, $\tilde{p} = p/p_o$ where p is the pressure in the same unit, S is the line strength and ν_o is the frequency of the line center. For a gas uniformly mixed in the atmosphere with a mass mixing ratio r, it follows that the optical depth of a layer between defined pressure levels p' and p'' is (e.g., Section 3.3c)

$$\tau_\nu = \frac{r}{2p_o g}\int_{p'}^{p''} \frac{Sp\alpha_{Lo}/\pi}{(\nu-\nu_o)^2 + \alpha_{Lo}^2 p^2}dp \tag{7.34}$$

and for absorption in the line wings where $\nu - \nu_o > \alpha_{Lo}p$,

$$\tau_\nu \approx \frac{k_o r}{g}[p''^2 - p'^2] \tag{7.35}$$

where $k_o = S\alpha_{Lo}/\pi(\nu-\nu_o)^2$. For an atmosphere in hydrostatic equilibrium, $p = p_o e^{-z/H}$ where H is the atmospheric scale height, and it follows from (7.35) that

$$t(z) = \tau^* e^{-2z/H} \tag{7.36}$$

where $p' = 0$, and $\tau^* = k_o r p_o / 2g$. Let us define the weighting function relative to the satellite altitude ($z = \infty$) as

$$\mathcal{W}(z, \infty) = \frac{dT}{dz}(z, \infty) \tag{7.37}$$

then substituting $\exp(-t)$ for $\mathcal{T}(z, \infty)$ and with (7.36) into (7.37), we obtain

$$\mathcal{W}(z, \infty) = \frac{d\mathcal{T}(z, \infty)}{dt}\frac{dt}{dz} = \frac{2\tau^*}{H}\exp\left[-\frac{2z}{H} - \tau^* e^{-2z/H}\right] \tag{7.38}$$

The characteristic relationship between $\mathcal{W}$ and z given by this simple formula is shown in Fig. 7.16a for three different values of τ^*. The shape of the weighting function is governed by two factors: the factor $\exp(-2z/H)$ which decreases with increasing z and the factor $\exp[-\tau^* \exp(-2z/H)]$ which increases as z increases. The first of these factors represents the decrease in absorber gas with changing z and the second factor characterizes the increase in transmission as the path decreases to 0 as z approaches the satellite altitude. These combine to produce a familiar bell-shaped weighting function curve. The width of this curve ultimately characterizes the vertical resolution of the retrieval (refer to Problem 7.5 as an example of this) and the peak of the curve occurs at

$$z_{max} = \frac{H}{2}\ln \tau^*$$

which follows by setting $d\mathcal{W}/dz = 0$. Therefore, measurements at different frequencies characterized by different values of τ^* allow us to sample the emission from different layers in the atmosphere. These layers broadly correspond to the layers that surround the peaks of the corresponding weighting functions. The physical interpretation of the general bell shape of the weighting function curves was discussed in Chapter 3. Near the line center, τ^* is large and the weighting function is more sharply peaked with a maximum higher in the atmosphere. As we move away from the line center toward the wings, τ^* decreases by virtue of the decreasing absorption coefficient. If far enough out from the line center, the maximum of the weighting function actually occurs at the surface (Fig. 7.16a).

The width of lines in the 15 μm CO_2 band varies from about 0.1 to 0.001 cm^{-1} over the range of atmospheric pressures of interest. Most radiometers measure the spectral intensity with a spectral

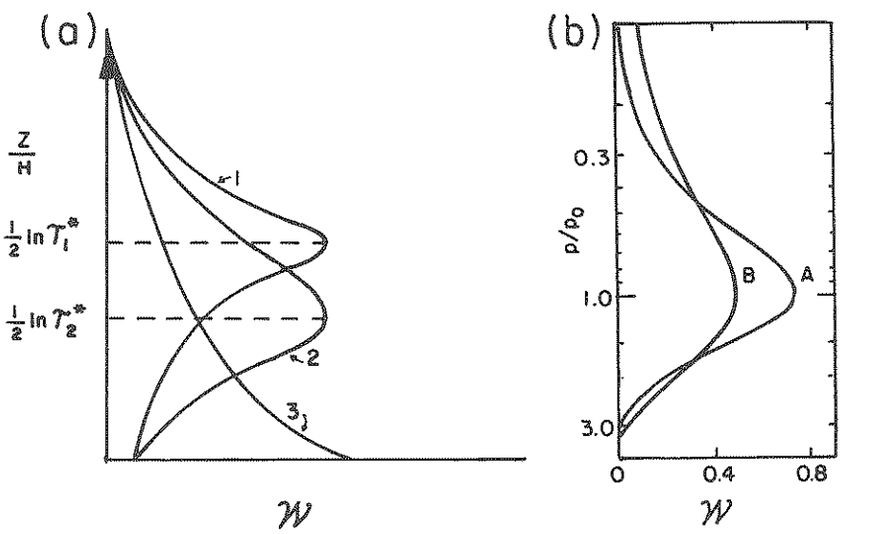

Figure 7.16 (a) The behavior of a monochromatic weighting function $\mathcal{W}$ in the wing of a collision broadened line corresponding to a hydrostatic atmosphere for different value ranges of τ^*, the total optical depth of the atmosphere. Curves labeled as 1: $\tau^* > 1$, 2: $\tau \geq 1$ and 3: $\tau^* \leq 1$. (b) The weighting functions for a monochromatic frequency in the wing of a collision broadened line (A), and for a nonmonochromatic band of frequencies containing strong absorption lines (B) (Houghton et al., 1984).

bandwidth that is significantly broader than the width of individual lines so the radiation actually detected by such an instrument results from the collective emissions by a band of hundreds to thousands of lines. The weighting function for a broad interval containing many overlapping absorption lines can be thought of as a superposition of weighting functions of individual lines each characterized by different values of τ^*. The result is a weighting function that is smeared out over several layers and one that is broader than a weighting function derived for single lines. Figure 7.16b provides an actual example of weighting functions calculated using a special type of transmission model to represent the absorption of a spectral interval that contains many spectral lines.

7.5.2 Weighting Functions for Zenith Sounding

The weighting functions characterizing the emission from the atmosphere as measured by an instrument on the ground looking up are very different from those for nadir viewing instruments. To exam-

ine the characteristic shape of these functions, consider the zenith intensity measured at the ground

$$I(\tau^*) = \int_0^{\tau^*} \mathcal{B}(t) e^{-(\tau^* - t)} dt \tag{7.39}$$

which follows from (7.6b) with $I(0, -\mu) = 0$. The transmittance $\mathcal{T}(\tau^*, t) = \exp[-(\tau^* - t)]$ assuming $\mu = 1$ which becomes

$$\mathcal{T}(z, 0) = \exp[-\tau^* + \tau^* e^{-2z/H}] \tag{7.40}$$

by virtue of (7.36). It simply follows that the weighting function

$$\mathcal{W}(z, 0) = \frac{d\mathcal{T}}{dz} = \frac{2z}{H} e^{-\tau^*} \exp\left[-\frac{2z}{H} + \tau^* e^{-2z/H}\right] \tag{7.41}$$

where the major difference between (7.41) and (7.38) is the change in sign inside the exponential, which leads to $d\mathcal{W}/dz < 0$ and predicts that the shape of the weighting function is always of the type labeled 3 in Fig. 7.16a regardless of the value of τ^*. Two factors also dictate the general shape of these weighting functions. The first of these factors, $\exp(-2z/H)$, characterizes the change in absorber with z and the second factor, $\exp[\tau^* \exp -2z/H]$, is the decrease of transmission as z increases upward away from the instrument. For the distribution of absorbing gas considered, an instrument looking up always receives most of its radiation from layers adjacent to the ground. In the line centers, this radiation originates almost exclusively from layers near the surface whereas radiation is received from higher up in the atmosphere for wavelengths located in the line wings although the maximum emission still occurs near the surface where pressure is greatest and the line is broadest.

7.5.3 Weighting Functions for Limb Sounding

An example of the geometric configuration for limb sounding is given in Fig. 7.17. The intensity measured at the satellite can be expressed as the integral of the emission along a line–of–sight that is defined at the tangent altitude h. We write this equation in the form

$$I(h) = \int_\infty^0 \mathcal{B}(s) \frac{d\mathcal{T}}{ds}(s, 0) ds \tag{7.42}$$

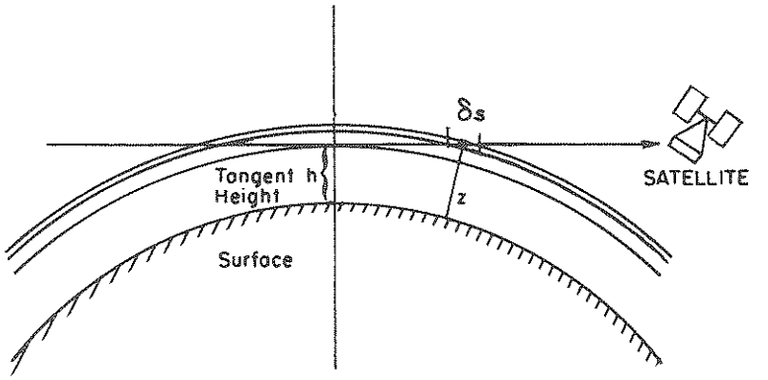

Figure 7.17 Limb viewing geometry. The satellite instrument scans through the atmosphere along the limb at a tangent height h. Intensity is received from segments δs of the path at height z.

where $\mathcal{T}(s, 0)$ is the transmission along the path of length s from the outer levels of the atmosphere at $s = \infty$ through the tangent height to the instrument at $s = 0$. As earlier, our analysis considers only the hypothetical case of monochromatic radiation whereas real applications deal with a frequency average over the band pass of the instrument. In reality, an instrument also has a finite field of view and measures the radiation over some finite vertical layer. In the case of vertical sounding, it is usually assumed that the intensity is uniform across the instrument field of view. Although this generally does not apply for limb sounding because the intensity typically varies rapidly across the field of view, it is nevertheless assumed here merely to simplify matters.

It is also possible to carry out a simple analysis of the properties of the weighting functions for limb sounders assuming a small field of view of the instrument and a single frequency response. We use the approach developed earlier for nadir sounding and rewrite (7.42) in the form

$$I(h) = \int_h^\infty \mathcal{B}(z') \frac{d\mathcal{T}}{ds}(z', \infty) \frac{ds}{dz'} dz' \tag{7.43}$$

where the integration is now over altitude z rather than over the tangent path s. We can relate s to z using simple geometric arguments to obtain the approximation

$$s^2 \approx 2R(z - h)$$

With a vertical weighting function defined as

$$\mathcal{W}(h;z,\infty) = \frac{d\bar{T}}{ds}(z,\infty)\sqrt{R/2(z-h)} \quad z > h$$

$$\mathcal{W}(h;z,\infty) = 0 \quad z < h, \tag{7.44}$$

then (7.43) becomes

$$I(h) = \int_h^\infty \mathcal{B}(z')\mathcal{W}(h;z',\infty)dz' \tag{7.45}$$

The square root factor in the definition of $\mathcal{W}$ represents the enhancement of the tangent path relative to a vertical path. Because of this factor, the tangent path defines an absorber amount that is several times larger than that of the vertical path. This enhancement of the absorber path increases the sensitivity of the emission from trace gases such as CO, NO, N_2O, and ClO providing the sensitivity necessary for sounding these gases.

To calculate the weighting functions relevant to limb sounders, the contribution to the measured intensity due to the emission by a layer Δz thick located at z is required. Assuming the geometry of Fig. 7.17, the emission from the layer located about height z follows from (7.43) as

$$\Delta I(z) = \frac{d\bar{T}}{ds}(z,\infty)\sqrt{R/2(z-h)}[e^{-\tau_1} + e^{-\tau_2}]\mathcal{B}(z)\Delta z \tag{7.46}$$

where

$$\tau_1 = r\int_z^\infty k_m(z')\rho_{air}(z')\sqrt{R/2(z'-h)}dz'$$

and

$$\tau_2 = \tau_1 + 2r\int_h^z k_m(z')\rho_{air}(z')\sqrt{R/2(z'-h)}dz'$$

Here the atmosphere has been divided into two regions; one is the region above the reference level z and nearer to the satellite than the tangent point and the other is that portion of the atmosphere behind the reference level including the path through the layer defined by h and z. τ_1 is the optical path for the first of these paths and τ_2 corresponds to the second and longer path. The factor of two results from the path symmetry about h through the layer defined by h

and z. Using the hydrostatic assumption, together with an assumed Lozentz line profile,[4]

$$\tau_1 = \frac{\tau^*}{2}\sqrt{\pi HR}[1 - \mathrm{erf}(\sqrt{2(z-h)/H})]\exp(-2h/H), \tag{7.47a}$$

and

$$\tau_2 = \tau_1 + \tau^*\sqrt{\pi HR}\ \mathrm{erf}(\sqrt{2(z-h)/H})\exp(-2h/H), \tag{7.47b}$$

where erf is the error function. The weighting function then follows from (7.45) and (7.46) as

$$\mathcal{W}(h;z,\infty) = \tau^*\sqrt{R/2(z-h)}\exp(-2z/H)[e^{-\tau_1} + e^{-\tau_2}]. \tag{7.48}$$

Figure 7.18a provides examples of this weighting function for different values of τ^*, with the tangent height $h = 12$ km and other parameters as given. For the larger optical depths, the emission arises from broad layers above the tangent height and closer to the sensor and the contribution from the layers near the tangent height is reduced. For $\tau^* = 0.1$, the main contribution comes from the layer immediately above the tangent height. In reality, the observations are obtained by operating in the optically thin region of the stratosphere and by scanning the sensor field of view. This offers a way of obtaining a high vertical resolution in the sounding. Figure 7.17b presents examples of actual weighting functions derived for a relatively wide spectral interval covering much of the 15μm band of carbon dioxide for various values of the tangent height h.

Some distinct advantages of limb sounding by emission are:

- Relatively high vertical resolution. None of the emitted radiation originates below the tangent point. From simple geometric arguments, the atmospheric shell immediately above the tangent height h contains the longest ray path of any layer and since pressure decreases exponentially with height, a large fraction of the outgoing radiation originates from a layer which is typically a few kilometers above the tangent height. As a result of these factors, the weighting functions are spiked.

[4] Note the assumption of a Lorentz line shape, which is used for convenience here, is not strictly appropriate since Doppler broadening mechanisms will also be important at typical stratospheric pressures and at the wavelengths of relevance to most limb sounders.

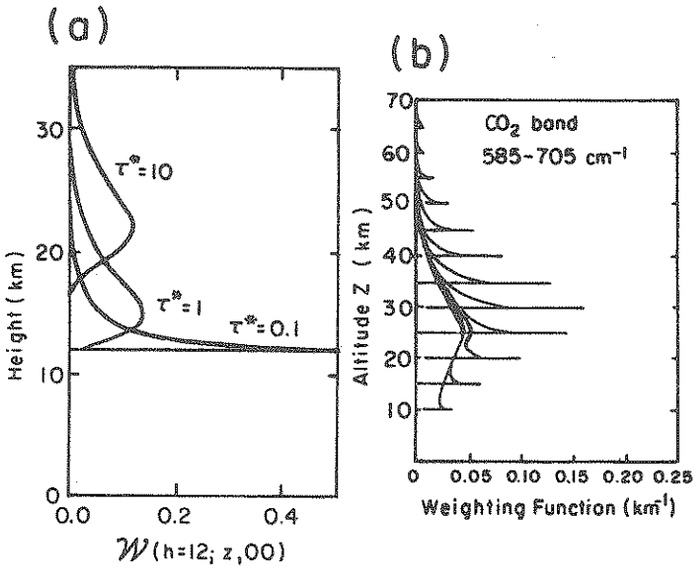

Figure 7.18 (a) The weighting function for limb sounding derived from (7.48) with H=7 km, R=6370 km, and h=12 km for three values of τ^*. (b) A set of weighting functions for a limb sounder based on the ideal case of an instrument with an infinitesimal vertical field of view. The weighting functions are computed for the spectral band 585–705 cm^{-1} which covers most of the 15 μm absorption band of carbon dioxide (after Gille and House, 1971).

- No surface influence on the measured intensities.
- Based on the geometry, considerably more emitting gas (up to about 60 times) exists along grazing paths than along vertical paths. This means that there can be significant contributions by the emission of gases of low concentration than occurs for along vertical paths.

The technique does have certain disadvantages. It is sensitive to the presence of aerosol in the lower stratosphere and generally cannot be reliably used to probe below the tropopause. Limb sounding also requires relatively precise information about the field of view and spacecraft attitudes so that instrument pointing can be accurately determined.

7.5.4 Weighting Functions of an Operational Sounder System

The NOAA TIROS–N Operational Vertical Sounder (TOVS) contains three sounders: the Microwave Sounding Unit (MSU), the

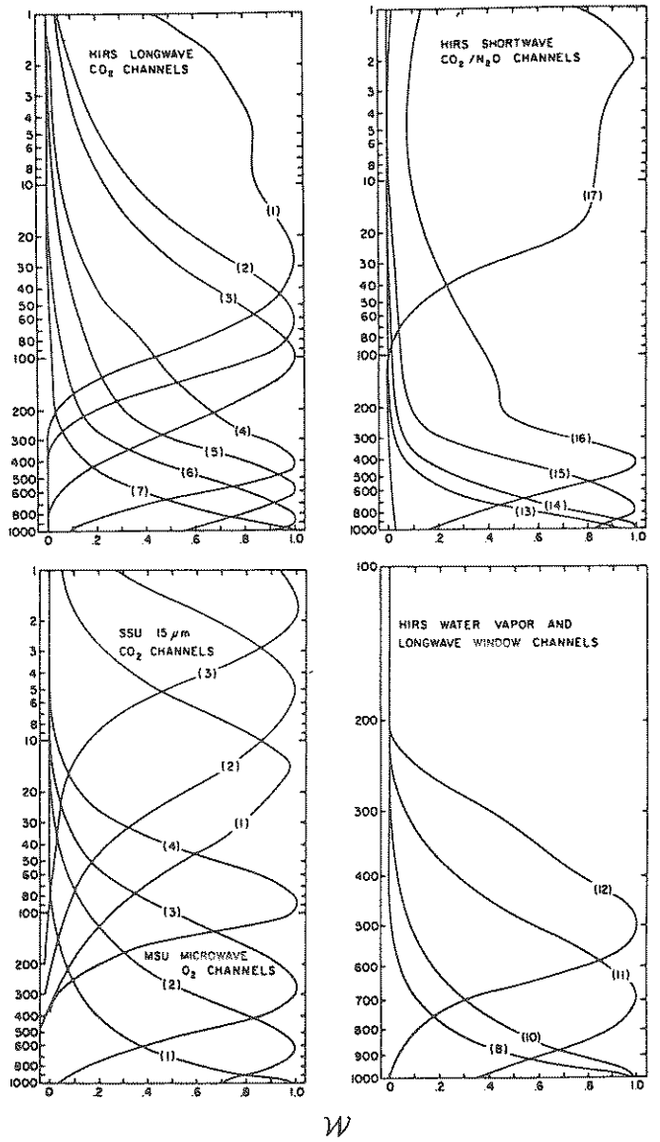

Figure 7.19 Weighting functions for the TOVS sounders (Smith et al., 1979).

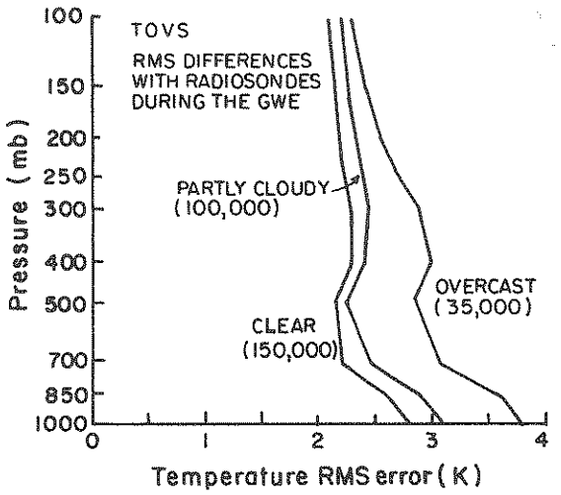

Figure 7.20 Root–mean–square differences between TOVS and radiosonde soundings for an entire year. The collocation and time differences are generally within 200 km and ± 3 hours (Smith, 1991).

High–resolution Infrared Radiation Sounder (HIRS), and the Stratospheric Sounding Unit (SSU). Figure 7.19 presents characteristic weighting functions for each sounder and illustrates the general features predicted by our simple analysis described above.

The actual numerical methods used to retrieve temperature from spectral measurements are not described any further here as these are summarized in some detail by Houghton et al. (1984) and other references noted later. These details are also the subject of the inversion project introduced in Appendix 2. A general assessment of the accuracy of retrieved temperatures is also provided in a number of studies and an example of such an assessment is presented in Fig. 7.20 in the form of the root–mean–square difference between the TIROS–N and radiosonde layer–mean temperatures. This rms difference is around 2–3 K for clear skies but is poorer for partially cloudy conditions and worst for overcast conditions. The reduced accuracy of the overcast sky retrievals is perhaps due to the limited number of tropospheric sounding microwave channels and their poor vertical resolution in the lower troposphere compared to the infrared channels. Although the rms differences of a few degrees shown in Fig. 7.20 seems small, individual differences from radiosondes may be as high as 10 K. These differences typically occur as a result of the coarse vertical resolution of TOVS soundings and the inability to re-

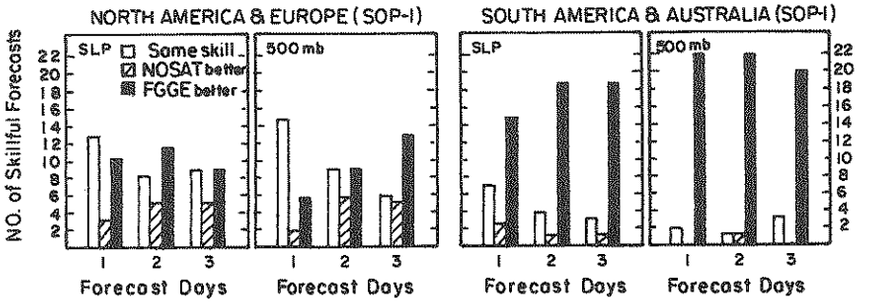

Figure 7.21 Number of cases of positive and negative forecast impacts of the FGGE observing system with and without satellite data during the period January 5 – March 5, 1979 (Kalnay et al., 1985).

solve sharp temperature gradients. Because of this problem, the rms difference between TOVS and radiosonde measured temperatures tend to be largest near the surface and near the tropopause where vertical temperature gradients are capable of varying significantly.

Many of the major operational forecast centers of the world, as well as a number of numerical modeling research laboratories, have investigated the impact of the TOVS data on numerical forecasts. The general findings from this research are conveniently summarized in Fig. 7.21 which is taken from the study of Kalnay et al. (1985). This diagram shows the number of times one of two observing systems, the FGGE, which includes satellite data, and the NOSAT, which excludes these data, led to a better forecast when compared to each other[5]. Whereas the results for the northern hemisphere are mixed, satellite data proved to be indispensable for analyses in low latitudes and in the southern hemisphere. Even in the northern hemisphere, satellite data improved the analyses over remote areas like the northern Pacific region and helped improve forecasts downstream of that region.

[5] FGGE is the acronym for the First GARP (Global Atmospheric Research Program) Global Experiment. One of the aims of this experiment was to develop an international observing system for studying the atmosphere and to test these systems during special observing periods throughout an operational year that began in 1978.

7.6 Sensing Clouds by Emission: Windows and Arches

The general topic of remote sensing of clouds has recently loomed as an important aspect of global climate change research. The field is not as highly developed as other topics of remote sensing discussed in this book although a number of new satellite initiatives through the 1990s is expected to accelerate research on this topic and produce new quantitative techniques for sensing clouds. Most of the existing methods unfortunately provide only gross and highly ambiguous properties of clouds (such as how much cloud exists, how often it occurs and some measure of an "effective" particle size among others). A method providing this type of information about cirrus clouds using infrared emission measurements will now be described.

Emission spectra between 9.1 and 16.7 μm measured by an interferometer flown on a high flying aircraft over a cirrus cloud of varying thickness are shown in Fig. 7.22. The feature to note from these spectra is how the emission, particularly in the window region, changes as conditions vary from clear to cloudy skies. The most obvious change is the decrease in emission as the optical thickness of the cloud increases, especially in the atmospheric window region between 10 and 13 μm. The radiation sensed by the instrument over thin cloud, for example, is a mixture of the radiation that is emitted below the cloud by the surface and underlying atmosphere and the radiation emitted by the cloud itself (both by the cloud particles and the emitting gases between these particles). A simple model of this mixture, given the assumption that scattering by cloud particles is negligible for these wavelengths, follows from (7.8) which can be written as

$$I_{obs}(0,\mu) = I_s e^{-\tau^*/\mu} + \mathcal{B}(T_c)[1 - e^{-\tau^*/\mu}] \qquad (7.49)$$

where $I_{obs}(0,\mu)$ is the intensity observed at cloud top, I_s is the upward intensity at cloud base, τ^* is the optical thickness of the cloud, and $e^{-\tau^*/\mu} = \mathcal{T}(\tau^*, 0, \mu)$ is the transmission through the cloud. This simple model considers the cloud to be isothermal at a temperature T_c. Since scattering is assumed to be negligible, it follows that

$$[1 - e^{-\tau^*/\mu}] = \mathcal{A}(\tau^*, 0, \mu) = \varepsilon(\tau^*, \mu)$$

where $\mathcal{A}(\tau^*, 0, \mu)$ is the absorptivity of the cloud (also known as the cloud emissivity). The stronger the absorption, the larger is τ^*, the

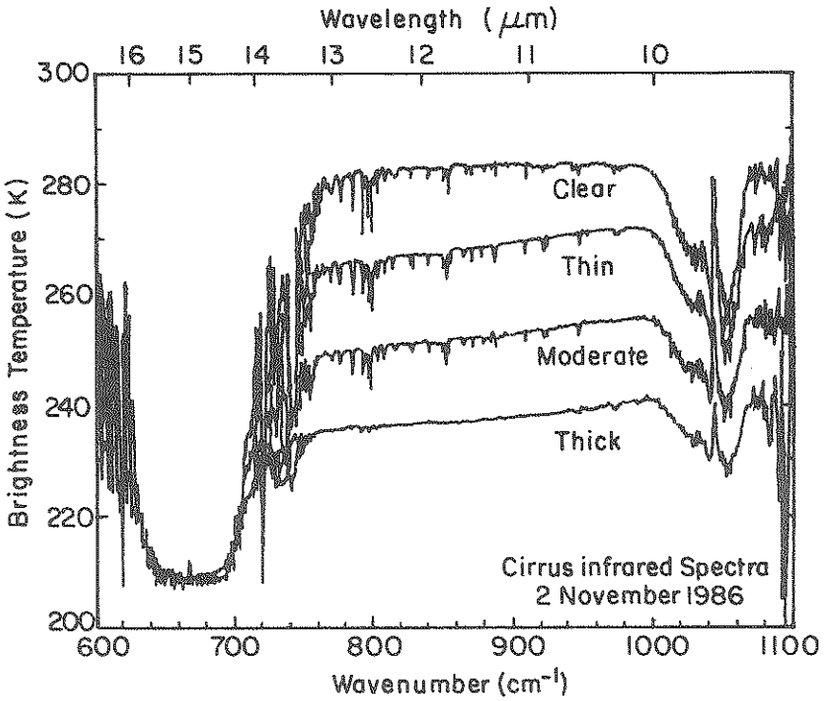

Figure 7.22 The emission spectra between 9.1 and 16.7 μm expressed in terms of brightness temperature measured over a clear scene and cloudy scenes of thin, moderate, and optically thick cirrus clouds observed by an interferometer on a research aircraft (Smith, personal communication).

closer ε is to unity and the smaller is the surface contribution to the observed intensity.

A second but less notable feature of the emission spectra shown in Fig. 7.22 is the change in the difference between the emission at 10 and 12μm and the relative change in this difference from clear to cloudy skies. A convenient way to study this change is to consider the slope in the emission spectrum from one wavelength, such as at 10.8μm to another longer wavelength such as at 12μm. The brightness temperature difference $\Delta T = T_{10.8} - T_{12}$ is a measure of this slope and is near zero both for clear skies and for overcast skies filled with optically thick clouds.[6] A plot of this temperature difference as a function of one of the measured brightness temperatures, say $T_{10.8}$, resembles an arch shape like that shown in Fig. 7.23. One

[6] This brightness temperature difference is 0, by definition, for blackbodies.

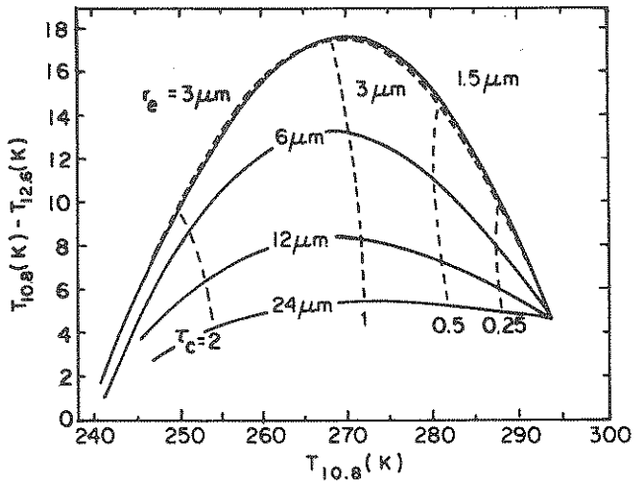

Fig. 7.23 Theoretical brightness temperature differences between 10.8 and 12.6μm as a function of the corresponding brightness temperature at 10.8μm for high level spherical ice crystal cirrus clouds as a function of effective radius and optical thickness (from King et al., 1992).

foot of the arch defines the temperature of clear skies and the other foot establishes the temperature associated with the emission by the densest portion of the cloud. The variation of ΔT between each foot depends on a number of factors including the size and shapes of the emitting ice particles and the optical thickness of the cloud. Figure 7.23 shows theoretically based calculations of the brightness temperature differences as a function of $T_{10.8}$ for calculations assuming spherical ice particles and a distribution characterized by different values of effective radius r_e and different values of optical thickness.

A convenient way to highlight the sensitivity of the emission spectrum to particle size is to invert (7.49) for optical depth

$$\tau^* = -\mu \ln[\frac{I_{obs} - \mathcal{B}(T_c)}{I_{clr} - \mathcal{B}(T_c)}] \tag{7.50}$$

where the clear sky intensity I_{clr} is substituted for I_s. The right–hand side of (7.50) can be evaluated using the measured intensities although estimating T_c is not easy for satellite applications. One approach to do this is to assume that this temperature corresponds to the intercept of the ΔT curve in Fig. 7.23 with the $T_{10.8}$ axis.

The clear sky intensity may also be estimated from observations of clear sky areas adjacent to the cloud (these areas correspond to the other foot of the arch in Fig. 7.23). Another way of estimating the clear sky brightness temperature is discussed later.

Having derived τ^* according to (7.50), the wavelength ratio

$$\gamma = \frac{\tau^*_{12.6}}{\tau^*_{10.8}} \tag{7.51}$$

is then established and we can see how this ratio depends on particle size by considering the following. In the absence of scattering (and in the absence of any molecular absorption both of which are reasonable assumptions for the wavelengths under consideration), the optical depth is

$$\tau^* = \pi \int Q_{abs} n(r) r^2 dr \Delta z$$

for spherical particles of radius r uniformly distributed throughout the cloud layer of depth Δz. For this specific case, and for a cloud composed of N_o particles of radius $r = a$,

$$\tau^* = \pi N_o a^2 Q_{abs} \Delta z$$

such that the optical depth ratio becomes

$$\gamma = \frac{Q_{abs,1}}{Q_{abs,2}}$$

The sensitivity of this ratio to particle radius a can be explored with the model for Q_{abs} introduced in section 5.5. Application of (5.58) leads to

$$\gamma = \frac{\mathcal{K}(n_1^2(1 - c_1^3)v_1)}{\mathcal{K}(n_2^2(1 - c_2^3)v_2)} \tag{7.52}$$

where

$$c_{1,2} = \frac{(n_{1,2}^2 - 1)^{1/2}}{n_{1,2}}$$

and where $n_{1,2}$ is the real part of the refractive index with the subscripts referring to the two selected wavelengths. For the specific example given later, the subscript 1 refers to λ =12μm and subscript 2 to λ =10.8μm. Figure 7.24a presents a plot of the relationship defined by (7.52) as a function of the particle radius a

Figure 7.24b presents γ derived from Lorenz–Mie theory and from scattering solutions for cylindrical particles as a function of particle radius. In Fig. 7.24a γ is expressed as a function of the radius of a single particle and of the effective radius r_e of an assumed size distribution in Fig. 7.24b. In each diagram, γ decreases rapidly to values near unity as a increases to 15 μm or as r_e increases to 20 μm at which point γ remains relatively insensitive to further increases in particle radius. The general variation of γ as a function of particle size can be understood in terms of the general dependence of Q_{abs} on the similarity parameter v as described previously in Section 5.5. Values of v_1 and v_2 corresponding to selected values of particle radius are given in Fig. 7.23a for reference. The lack of sensitivity of γ for large particles occurs when values of both v_1 and v_2 are large enough (in this case both exceed unity) such that Q_{abs} approaches the large particle asymptotic limit where $Q_{abs,1} \approx Q_{abs,2}$.

The problem with the approach described here for sensing ice particle size, and one common to most passive methods for sensing ice crystals, is that the measured brightness temperature differences are sensitive to the size of the crystals as well as to their shape and other factors. Unfortunately, it is generally not possible to separate these effects unambiguously. Methods to derive ice crystal size in terms of spheres of some equivalent radius and any subsequent interpretation of this size should be viewed cautiously. Another factor of relevance to the approach described earlier is that scattering of infrared radiation is not entirely negligible and the quantity γ is itself ambiguous and not necessarily a measure of the ratio of absorption optical depths as assumed earlier.

Excursus: Golden Arches

One of the advantages of satellites as observational platforms of clouds is their ability to record patterns and structures of clouds over wide ranges of space and time. A method that exploits this particular advantage, as well as using the properties of cloud emission, is the spatial coherence technique introduced by Coakley and Bretherton (1983). The idea behind the approach is portrayed in the upper panel of Fig. 7.25 which schematically presents a group of 2×2 neighboring pixels of 11μm radiances expressed in this specific example as brightness temperature. These pixels are processed to provide the average 11μm brightness temperature of the group and the standard deviation about this average. The latter is a measure

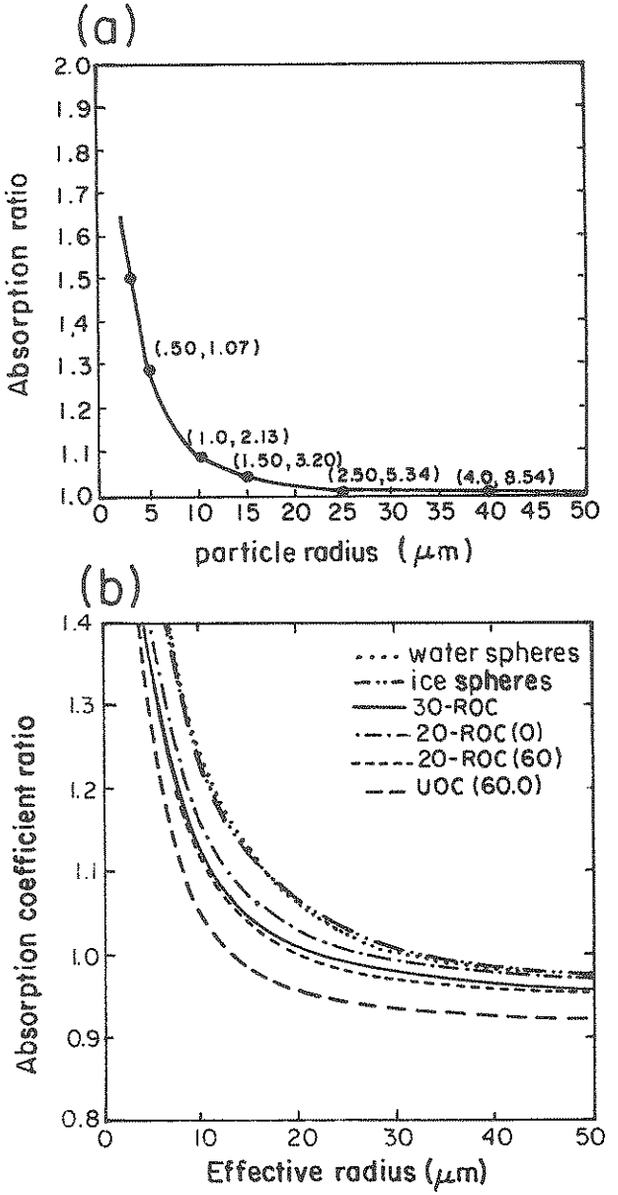

Figure 7.24 (a) The ratio of the absorption coefficient γ as a function of particle radius a. The values of v_1 and v_2 correspond to a single particle of specified radius with the refractive index 1: λ=10.8, m= 1.0905–i0.1710, 2: λ= 12, m=1.2457–i0.4023. (b) The results of Parol et al. (1991) for γ as a function of effective radius r_e for water and ice spheres and different orientation averages of ice cylinders.

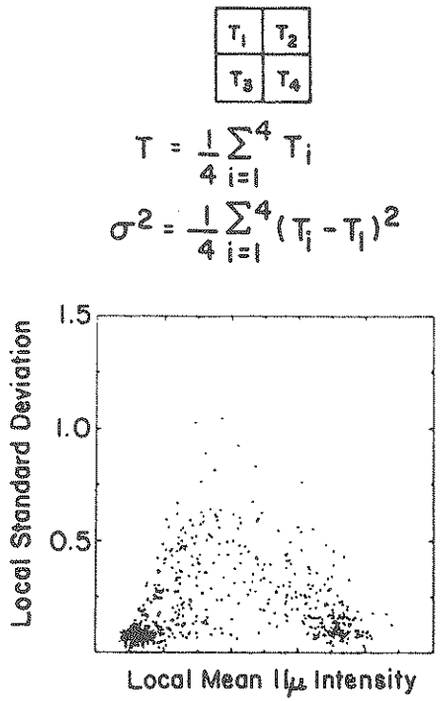

Figure 7.25 A schematic demonstration of the method of spatial coherence (upper panel) as it might be applied to brightness temperatures. Spatial coherence analysis of 11μm intensities for a (250 km)^2 region over stratus clouds off the west coast of California. Each point represents values for a 4×4 array of (1 km)^2 AVHRR pixels (Coakley, 1991).

of the texture of the image on the scale of the pixel array chosen. These two pixel group quantities are then plotted on a scatter diagram in the fashion given by the example of Fig. 7.24b. The satellite data used to construct this scatter plot are the 11μm radiances obtained with the NOAA–9 overpass at 2242 GMT on July 7 obtained from the AVHRR viewing marine stratus clouds off the west coast of California (Coakley, 1991).

The scatter of points on the diagram resembles an arch. The feet of the arch contain important information about those regions of the image that are relatively homogeneous across the group of neighboring pixels. One foot is associated with the relatively clear

sky portion of the scene and the other to the pixel groups that are completely filled by a cloud with the same temperature. This provides a way of discriminating clear sky brightness temperatures (T_{clr}) from partially cloudy skies (T_{broken}) and from the brightness temperature (T_{cld}) of a homogeneous layered cloud. For the case shown, only two effectively homogeneous surfaces exist, one is the clear sky background and the other is that of the solid cloud portions of the image. The points in the arch correspond to a partially filled pixel group of cloud cover N and it is assumed that these points can be expressed as

$$T_{broken} = (1 - N)T_{clr} + NT_{cld} \tag{7.53}$$

from which the cloud cover follows

$$N = \frac{T_{broken} - T_{clr}}{T_{cld} - T_{clr}}$$

Application of this approach alone provides limited quantitative information about clouds and applies only to single layer clouds. The approach relies on the empirical relationship (7.53) and on the statistical nature of the observations that can be used to identify both T_{clr} and T_{cld}.

7.7 More on Clouds: Slicing up the Atmosphere

Another approach for sensing cloud amount and the height of clouds (or specifically cloud top pressure) is the method referred to as CO_2 slicing. This method has been used by Wylie and Menzel (1989) to study cirrus clouds although the idea was described much earlier by Smith et al. (1974), McCleese and Wilson (1976) and others. The slicing method seeks to take advantage of differences of the absorption of the atmosphere at several spectral regions within one of the CO_2 molecular absorption bands. Whether clouds appear in images of these channels depends on the particular channel and the altitude of the cloud. Figure 7.26 gives examples of three weighting functions corresponding to three CO_2 channels of the VAS. Only clouds that emit radiation above the 350mb level contribute significantly to the radiance measured by the satellite in channel 3, whereas channel 4 is capable of differentiating the emission by clouds from that of the molecular atmosphere down to 700mb.

The method of CO_2 slicing begins with the radiative transfer equation

$$I(p,\mu) = I(p_s,\mu)\mathcal{T}(p_s,p,\mu) + \int_p^{p_s} \mathcal{B}(p')\mathcal{W}(p,p')dp' \tag{7.54}$$

occurs higher up and only emission by higher level clouds produces any significant effect on the intensity relative to clear sky intensities.

Figure 7.27b illustrates the cloud–top function calculated numerically from (7.57) assuming more realistic atmospheric profiles of temperature and humidity and two channels of the HIRS (channels 6 and 7). This diagram helps emphasize some of the problems in using the slicing method in polar regions where low–level temperature inversions occur. The variation of this function with pressure under these conditions is complicated. The existence of a temperature inversion below 700 mb in this profile causes cloudy sky intensities to exceed the clear sky intensities so that G exceeds unity. Lower in this atmosphere, a point is reached where the temperature of the cloud and ground approach one another such that $\Delta I_2 \rightarrow 0$ and $G \rightarrow \pm\infty$. This occurs between 800–850 mb in the example given in Fig. 7.27b.

The approach of Wylie and Menzel (1989) is to calculate $G(p_c)$ using temperature and moisture data representative of the region of interest and to estimate the cloud pressure from the ratio of observed intensities of two VAS channels. A comparison of their approach with cloud–top pressures deduced from lidar and from stereo parallax analyses is given in Fig. 7.28. The VAS cloud–top pressures typically exceed the lidar estimates by 70 mb. This comparison serves to emphasis the ambiguity of cloud–top pressure itself and how this quantity in fact may have a different interpretation depending on how it is derived. In the case of intensity slicing, it is assumed that the cloud occupies a thin layer defined by a unique value of p_c. In reality, the radiation emerging from cloud–top is the accumulation of radiation emitted throughout the depth of the cloud as well as transmitted from below the cloud. A simple way of viewing this radiation is to consider that it originates from some effective level below cloud–top. This level only approximates the cloud top surface for the densest portions of the cloud.

7.8 Intensity Classification of Clouds

Clouds provide a first–order effect on the radiative budgets and water exchanges in the atmosphere. They also play a fundamental role in studies of climate and climatic change. Several attempts have been made to classify the global distribution of clouds based on measurements obtained from radiometers flown on satellites. Two examples of these radiometric classifications of clouds will now be discussed.

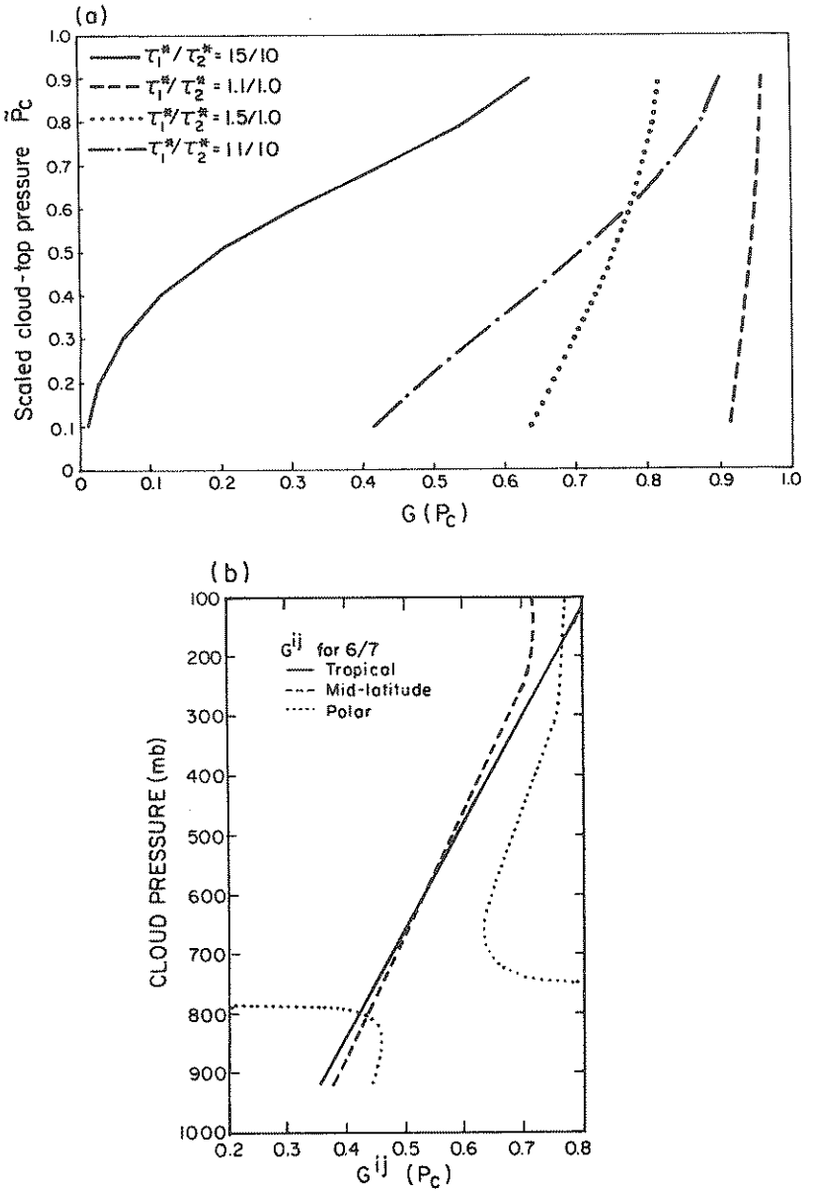

Figure 7.27 (a) The cloud–top pressure function as derived from (7.56) for the following ratios of $\tau_1^* : \tau_2^*$ curve 1 1.1:1.0, curve 2 1.5:1.0, curve 3 11:10, and curve 4 15:10. (b) The cloud–top pressure function calculated for ratios of channels 6 and 7 of the HIRS (the channels centered on 13.64 and 13.25 μm) using tropical, midlatitude, and polar climatological temperature and moisture profiles (Wielicki and Coakley, 1981).

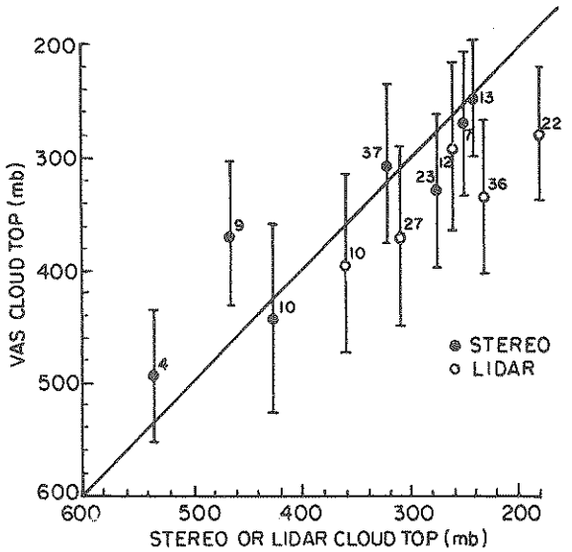

Fig. 7.28 The mean and standard deviation of all VAS cloud–top pressure data compared to lidar and satellite stereo cloud–top pressures. The error bars are 1 SD from the mean for the VAS derived pressures (Wylie and Menzel, 1989).

7.8.1 Emission Classification in the Split Window

Inoue (1989) developed a simple way to classify clouds according to the difference in their emission properties at 11 and 12 μm. As mentioned earlier, $\Delta T = T_{10.8} - T_{12}$ is a good indicator of the opacity of clouds. Thick clouds, radiating approximately like a blackbody, possess small values of ΔT whereas thin clouds exhibit more variable values of ΔT as described earlier in a way that depends on particle size and other factors.

Inoue's classification scheme is based on threshold analyses of the $T - \Delta T$ diagram like that shown in Fig. 7.23 and an example of this scheme is shown in Fig. 7.29. Two threshold values of ΔT can be identified, one at $\Delta T = 1$ K corresponding to optically thick clouds and another is set to a slightly larger value corresponding to the clear sky value of ΔT. Two thresholds values of the brightness temperature $T_{10.8}$ are also introduced in the Inoue scheme; one is the high cloud threshold which is set at -20° C and the other corresponds to clear sky temperatures. Data representing different cloud types fall in the different classification boxes. For example, cumulonimbus

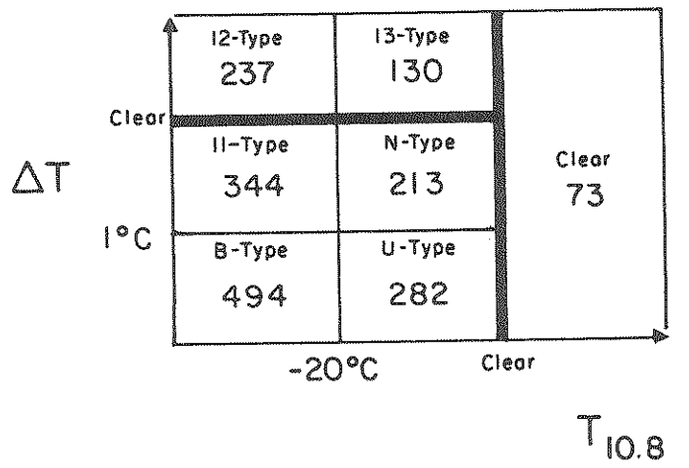

Figure 7.29 An example of a cloud type classification diagram introduced by Inoue (1989).

clouds are thick, possess ΔTs less than 1 K, and are cold. These fall in the type B category. Low level cumulus and stratocumulus clouds fall into Inoue's category U. Thin cirrus clouds are characterized by values of ΔT that exceed the clear sky threshold value and fall in categories I2 and I3 for thick and thin clouds respectively.

7.8.2 The International Satellite Cloud Climatology Project (ISCCP)

ISCCP formerly began in 1983 with the collection of the first internationally coordinated satellite intensity data. The original plan called for this collection for only a five–year period but the ISCCP has since been extended to 1995. This program was the first of its kind involving routine collection of operational satellite data. Many key problems needed attention, and these are will now be highlighted since they offer important lessons to the remote sensing of the atmosphere on the global scale.

Data Coverage and Data Management

Obtaining global coverage of cloudiness using satellite observations, while resolving diurnal variations of cloudiness, is difficult. The ISCCP notionally planned to make use of data from five geostationary satellites as well as data from a single polar orbiter in an effort to fill in the data voids over polar regions. Actual coverage during the first

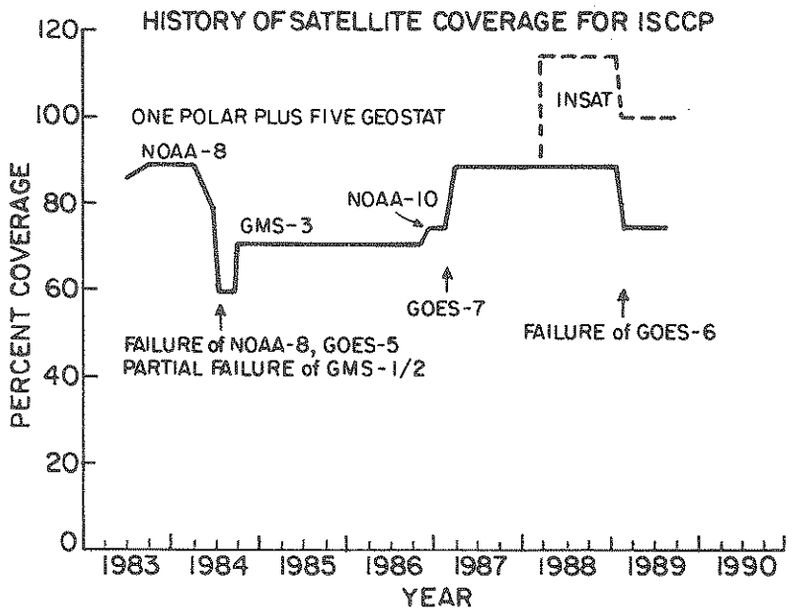

Figure 7.30 History of satellite coverage for the ISCCP. The coverage is defined to be at 100% for five geostationary satellites and one polar orbiter satellite, representing eight observations per day (although the actual observation frequency is smaller for polar orbiters). The initial complement of satellites included the NOAA–7, METEOSAT–2, GMS–2, GOES–5, and GOES–6. Failures and replacements of satellites are indicated. Time is given in quarter years (from Rossow and Schiffer, 1991).

six years of the ISCCP, measured against this hypothetical ideal of six satellites, is presented in Fig. 7.30. Because of the loss of satellites throughout this period, coverage was limited to about 90% for about three of the six years although with the availability of INSAT data, the data coverage could exceed that originally sought for ISCCP. Figure 7.30 graphically highlights the difficulty in providing observations of the global atmosphere and provides a commentary on those programs that propose to do so using single satellite platforms.

Satellite Radiance Calibration

The NOAA–7, 8, and 9 polar orbiting satellites provide ISCCP with AVHRR imagery data. These data play a crucial role in the ISCCP. They not only provide a completion of the data coverage over the poles and other regions that are not covered by geostationary satellites but the multispectral observations of the AVHRR also offer the potential for better analysis of clouds, such as cirrus and polar stratus clouds, that are difficult to identify with visible and far–infrared radiances. Perhaps the most important application of AVHRR data lies in its use as an intersatellite calibrator of radiance data. The procedure is to compare data routinely from each geostationary satellite and the afternoon NOAA polar orbiter, and normalize all radiance measurements to a single satellite. This normalization is then adjusted to that of the NOAA–7 in July 1983 as a way of monitoring long–term drifts during the lifetimes of the different satellites. Absolute calibration of this NOAA–7 standard is provided by aircraft measurements over a well–defined reflecting desert surface (Whitlock et al., 1989).

Figure 7.31 portrays the history of VIS and IR calibrations over the first five years of the project. The corrections that were required for the NOAA–9 visible radiances are shown in Fig. 7.31a. According to Fig. 7.31b, output from the IR channel varies with time and the operational calibration procedure generally corrects for these changes with only a small adjustment necessary from late 1987 through 1988.

Cloud Detection and Analyses

The cloud detection scheme is different from that described above and uses both visible reflection information and emitted radiation. The detection approach examines all of the data for one month to collect statistics on the space/time variations of the VIS and IR intensities. The key assumptions used in the analysis are that the intensities in clear scenes are less variable than those in cloudy scenes and that it is the clear scenes that compose the darker and warmer parts of the VIS and IR intensity distributions, respectively. Estimates of the clear sky values of VIS and IR intensities for each location and time are made and composited into maps (these are referred to as the "clear sky composites"). This approach is novel in two respects. First, all of the complicated tests usually used to detect cloudiness directly, many of which were first proposed by other investigators, are used here to identify clear scenes. The use of time variations at one location to identify clear scenes also differs from many other methods .

The differences between the intensities measured and the estimated clear sky intensities are compared to the uncertainties in estimating the clear intensities. If the differences are larger than

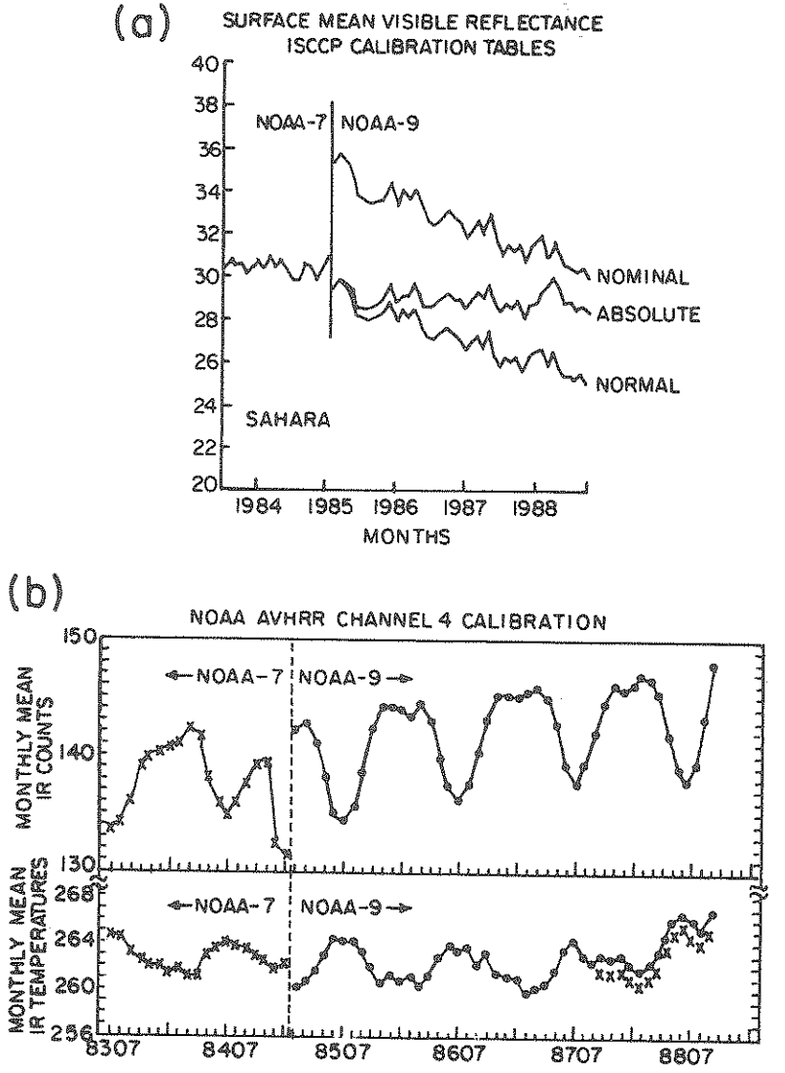

Figure 7.31 History of the AVHRR (a) visible channel and (b) the IR channel 4 for the NOAA–7 and NOAA–9 satellites. The nominal calibration is the calibration originally supplied by the satellite operator; the normalized calibration is that used to match NOAA–9 to NOAA–7 and the absolute is the final adjustment. The IR calibration is illustrated by showing the global, monthly mean IR brightness temperatures (from Rossow and Schiffer, 1991).

this uncertainty and in the "cloudy direction" at either wavelength (colder IR or brighter VIS), then the pixel is labeled cloudy. Once each pixel is classified as clear or cloudy, the measured intensities are compared to radiative transfer model calculations that include the effects of the atmosphere, surface and clouds. The intensity data are then converted into two cloud properties— the "visible" optical thickness (defined at 0.6 μm) and a cloud–top pressure. The optical thickness parameter determines the amount and angular distribution of sunlight reflected by the cloud layer (the full effects of multiple scattering are included in the model)— the cloud–top pressure is supposed to account for cloud emissivities less than 1. At night, when only IR intensities are measured, no cloud optical thickness is reported and IR variations are associated with the cloud–top brightness temperature.

Thus, the ISCCP clouds are categorized in terms of cloud–top pressure and optical depth properties as schematically shown in Fig. 7.32a. Two examples of this two–dimensional distribution for July 1983 are presented in Figs 7.32b and c for two different latitude zones. In the subtropics during winter (Fig. 7.32 b), the predominant cloud type has low tops and relatively low optical depths (probably associated with highly broken cloud). The tropical distribution is more complicated showing a prevalence of high, optically thick clouds and low, relatively thin clouds associated with highly broken low–level cloud.

7.9 Notes and Comments

7.1. The radiative transfer described in this chapter and the remote sensing methods based on this transfer ignore scattering processes. This is clearly a valid assumption when we consider only the transfer of infrared and microwave radiation in a molecular atmosphere but it is not always valid when dealing with transfer in clouds. In the infrared, scattering by clouds tends to be less dominant that the absorption and emission be cloud particles but it is not always negligible especially when a very cold cloud overlies a warm underlying surface (Stephens, 1980). Scattering by ice particles in the microwave becomes an increasingly important consideration as the frequencies increase beyond approximately 80 GHz.

7.2. A basic issue for almost all radiometric studies of the troposphere and the underlying surface is the need to establish clear sky intensities and thus determine whether a scene contains cloud. This

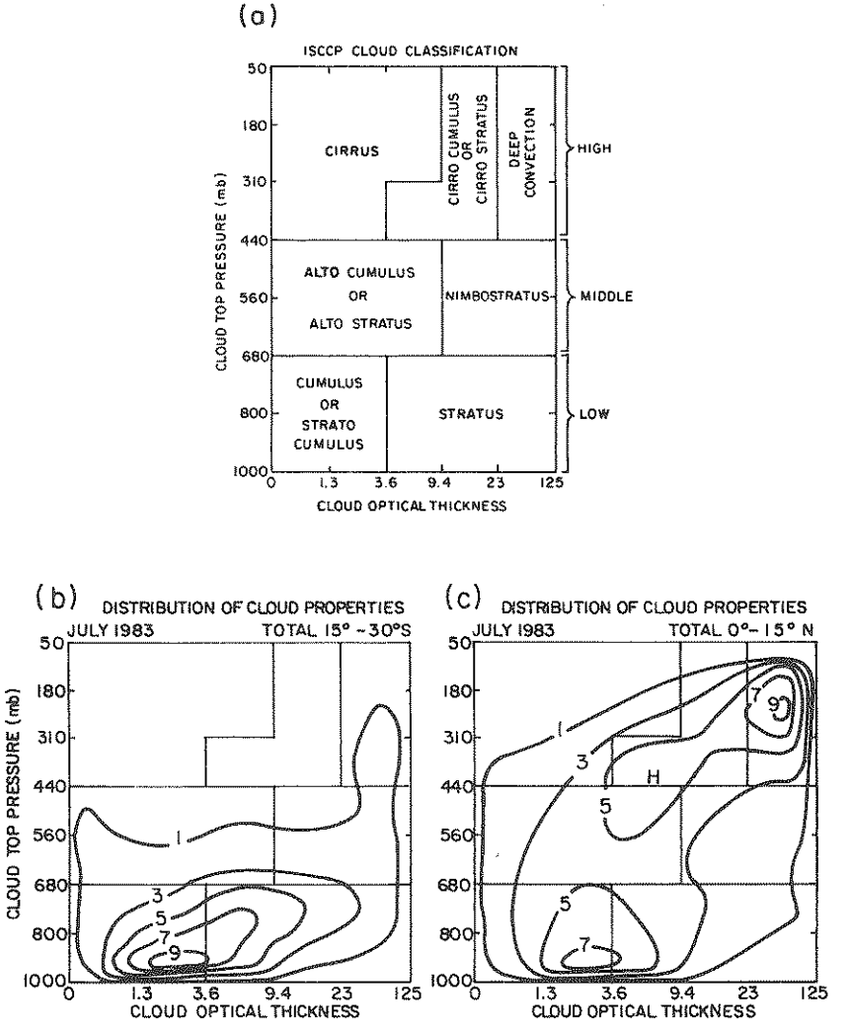

Fig. 7.32 (a) Radiometric classification of cloudy pixels in terms of optical thickness and cloud–top pressure. (b) The frequency distribution of cloud optical thickness and cloud–top pressure for July 1983 for the southern subtropics and (c) the northern tropics (from Rossow and Schiffer, 1991).

is the first step required in sensing the surface (this section), sounding the atmosphere (Section 7.5), and studying and classifying clouds (Sections 7.6–7.8). Different ways of establishing the clear sky intensity threshold exist, and some of these are described in Sections 7.7 and 7.8. One method that is used operationally as part of TOVS sounding is the cloud clearing scheme of McMillan and Dean (1982) which masks clear sky pixels so that data from these pixels can be subsequently used in soundings and SST retrievals.

An interesting but more difficult problem is the remote sensing of land surface temperature. The problem is that the emissivities of these surfaces (both their spectral and angular variation) is not well known [Prata (1993) and references therein].

7.3. A number of different methods exist for the retrieval of PWC from the SSM/I. Some are Alishouse et al. (1990), Schluessel and Emery (1990), and Petty and Katsaros (1990). Early microwave measurements from the Cosmos 243 satellite (Basharinov et al., 1969) determined total water content over the oceans from observations at 1.35cm wavelength. Measurements on and near the water vapor absorption line at 22 GHz were also obtained from the NEMS on the Nimbus 5 satellite (Staelin et al., 1976), SCAMS on Nimbus 6 (Grody et al., 1980), the SMMR on Nimbus 7 (Prabhakhara et al., 1982) before the SSM/I. The PWC has also been inferred from infrared sensors on satellites (such as from the IRIS instruments on the Nimbus 3 and 4; Conrath, 1969; Prabhakara et al., 1979).

7.4. A general overview of the methods for deriving rainfall from space sensors is given by Browning (1990). The OLR–precipitation approach described in this section forms the basis of the Global Precipitation Climatology Project (GPCP) under the sponsorship of the World Climate Research program (WCRP). The GPCP is also examining ways of merging the OLR methods and the passive microwave methods of precipitation retrieval.

The general concept for the remote sensing of hydrometeors from microwave emission measurements was suggested by Buettner (1963) and explored with aircraft observations by Singer and Williams (1968) and Kriess (1969) among others and quantified by Wilheit and collaborators during the late 1970s and 1980s (Wilheit et al, 1977; Wilheit, 1986) and Adler and Rodgers (1977). This is now a vigorous topic of research (e.g., Adler et al., 1991, Mugnai et al., 1990, and Kummerow et al., 1989) spurred on by the Tropical

Rainfall Measurement Mission (TRMM) to be launched in the late 1990s (Simpson et al., 1988).

The microwave methods described in this chapter are based on measuring the emission from the rainfall. These measurements are typically made around 19 GHz or so. Other passive microwave methods exist based on scattering of microwave radiation at higher frequencies. These methods, like that of OLR, are more indirect in that the radiation sensed by the radiometer is modulated by scattering from the ice particles at cloud–top. This is an interesting approach and requires a combined understanding of both emission and multiple scattering which is a topic that is not discussed in this book. An example of the method is contained in the work of Spencer et al. (1989). A principal advantage of the approach is that it applies equally well over land and ocean unlike the microwave emission approaches. Spencer (1993) has also introduced a largely empirical scheme for retrieving global rainfall from the emission sensed in the 60 GHz oxygen band by the MSU instrument.

7.5. Atmospheric sounding was one of the main motivations of the meteorological satellite program. Even before SPUTNIK, it was recognized that air temperature observations might best be made on a global scale using radiometric measurements from a satellite (King 1958; Kaplan 1959; Houghton 1961). In the United States, two experiments were developed in the 1960s for flight on the NIMBUS 3 experimental weather satellite: (1) a Michelson interferometer, called IRIS (refer to Chapter 3 for further discussion of this instrument), (2) a grating spectrometer called SIRS which measured radiation in eight distinct spectral bands selected specifically for temperature sounding. The SIRS absolute radiometric accuracy of 1 % and signal–to–noise ratio of 4000–1 was a phenomenal achievement for its time.

A major problem with the SIRS data was created by its large geographical field of view (225 km square). It is estimated that clouds interfered with the measurements more than 90% of the time. In order to account for the influence of cloud, a radiative correction to the measurement was calculated using a "guess" temperature profile and the tropospheric radiance observations (Smith et al., 1970). The guess profile was generated from statistical relationships with uncontaminated stratospheric–channel radiances. Although the procedure gave reasonable results for a single layer of cloud when the guess profile was close to the true profile, the cloudy–condition retrieval were in fact unreliable, and to a degree dependent on the cloud situation.

The TIROS–N satellite, the first of the current series of operational polar–orbiting satellites, was launched into orbit on October 13, 1978, just prior to the initiation of the FGGE. The second spacecraft in the series, NOAA–6, was launched into orbit on June 27, 1979, midway through the FGGE year.

An excellent overview of the topic of satellite sounding, including its historical perspective, limitations, and impacts is given in the review article of Smith (1991). A text largely devoted to sounding is that of Houghton et al. (1984). An excellent review of the topic of sounding inversion, including definition of resolution and other issues, is found in Rodgers (1976).

7.8. A plan to study clouds within the perspective of global climate was laid down at a meeting in Oxford in 1978. This plan identified a program to address a number of key problems associated with the role of clouds in climate and became known as the ISCCP. The basic idea of this project is a simple one, namely to make use of the international network of geostationary satellites to provide a satellite–based climatology of cloudiness. The goals of the project are:

- To produce a global, reduced resolution, calibrated, and normalized infrared and visible intensity data set, along with basic information on the radiative properties of the atmosphere, from which cloud parameters can be derived.
- To coordinate basic research on techniques for inferring the physical properties of clouds from satellite intensity data.
- To derive and validate a global cloud climatology
- To promote research using ISCCP data to improve parameterizations of clouds in climate models.
- To improve our understanding of the Earth's radiation budget (defined at the top of the atmosphere and at the surface) and hydrological cycle.

Important references describing ISCCP through its formative stages and its many aspects are conveniently summarized in Rossow and Schiffer (1991). Rossow and Garder (1992) describe the ISCCP cloud detection scheme in more detail than described in this book and Brest and Rossow (1989) discuss the topic of calibration of the AVHRR which is used as an intercalibration of radiometers on different geostationary satellites.

7.10 Problems

7.1 Explain or interpret the following:

a. In Fig. 3.26, emission spectra measured by an interferometer on the ground and by an interferometer on an aircraft are shown. What gross inferences about the vertical distribution of temperature can you make by studying these spectra?

b. The AVHRR instrument has a channel centered at 3.9μm which is also located in an atmospheric window. A satellite image of a cloud generally appears colder than its immediate surroundings at night but warmer than its surroundings by day.

c. Measurements of emission from the atmosphere at 15μm at a spectral resolution typical of that provided by an interferometer, in principle, yields higher vertical resolution sounding relative to an instrument that measures this emission over relatively broad channels.

d. Low clouds emit more infrared radiation than high clouds of comparable optical thickness.

e. The relative change in emission by thin clouds across the 10–13μm window region compared to a clear sky background emission varies according to the size of the cloud particles.

f. For the same total column optical thickness, the weighting functions of water vapor are more peaked than corresponding weighting functions for CO_2.

g. Qualitatively, what is the nature of the weighting function corresponding to emission in the 9.6μm band for measurements at the ground?

h. The "effective" level of emission determined from the brightness temperature of an optically thin cloud layer may actually not reside within the cloud layer itself.

7.2 Derive (7.9) and (7.10) from (7.6b) and (7.6a), respectively, assuming that

$$\mathcal{B}(\tau) = \mathcal{B}_o + (\mathcal{B}^* - \mathcal{B}_o)\tau/\tau^*$$

7.3 Assume a Lorentz line shape for the 22.235 GHz water vapor line. On the line center,

a. Show that the optical depth due to water vapor is

$$\tau^* = \frac{k_o r_s p_s}{3g}$$

where $k_o = S/\pi\alpha_s$, α_s is the line half–width defined at the surface pressure p_s and r_s is the surface value of mixing ratio. Assume the form $r = r_s\tilde{p}^3$ in your derivation where $\tilde{p} = p/p_s$ (compare this with Problem 3.7).

b. Using the results obtained from Problem 3.7 (a), express this optical depth as a function of precipitable water content w.

c. Using (7.23), estimate T_b for five values of w assuming 1-ϵ=0.6, $\mathcal{T}_{OX}$=0.98, and $k_o = 1 \times 10^{-2}$ m^{2}kg^{-1}. Use the 5 values of T_s and corresponding values r_s listed in Table 3.2, the latter based on a surface relative humidity of 70 %.

7.4 Repeat the analysis but assume the measurements are at a frequency in the wing of the absorption line. Assume this frequency to be 19 GHz and express your answer in terms of $k_o = S\alpha_s/\pi(\nu - \nu_o)^2$ and assume a value of 4.15×10^{-3} m^{2}kg^{-1} for this quantity.

7.5 The volume absorption coefficient of the water vapor line at 22 GHz is approximated by

$$k \approx 6 \times 10^{-3}\rho_v \left(\frac{300}{T}\right)^2 \text{ km}^{-1}$$

where ρ_v is the water vapor density in gm^{-3}, and T is the temperature in Kelvin. A commonly used standard atmosphere has the properties

$$\rho_v = \rho_o e^{-z/2}$$

$$T = T_o - 6.5z$$

where z is in km and ρ_o and T_o are sea–level values (say 1.19 kgm^{-3} and 292 K). Assuming the atmosphere lies in the lowermost 10 km, calculate the brightness temperatures at 22 GHz observed by an instrument at the top of the atmosphere looking down and at the base of the atmosphere looking up.

7.6 Consider a downward–looking, nadir– pointing radiometer observing the ocean surface from an airborne platform above a 2

km thick cloud with a water content $w = 1.5\text{gm}^{-3}$. The volume absorption coefficient of water is given approximately by

$$k_v = 2.4 \times 10^{-4}\nu^{1.95}w \qquad \text{km}^{-1}$$

where ν is in GHz and w gm^{-3} . For an ocean brightness temperature of 150 K, calculate and plot the observed brightness temperature as a function of frequency from 1 to 30 GHz assuming the physical temperature of the cloud is 275 K. For this exercise, ignore the effects of water vapor absorption and compare your answer at 22 GHz with your answer for Problem 7.5.

7.7 A simple measure of the vertical resolution of a single sounding channel may be defined as

$$\Delta z = z_{max} - z_{1/2}$$

where z_{max} is the height of the maximum of the weighting function and $z_{1/2}$ is one of the heights corresponding to the altitude where the weighting function is half its maximum value. Following the analysis presented in Section 7.5 (a), show that $z_{1/2}$ is obtained from the solution of

$$\frac{H}{2}\tau^* e^{-2z/H} + z = \frac{H}{2}\ln[2e\tau^*]$$

for z. Solve this equation and obtain an estimate of Δz assuming $H = 8$ km and values of $\tau^* = 0.1$, 1, and 10. *[Hint: The solution to the equation*

$$ae^{-bx} + x = c$$

has the form

$$x = \frac{W(-abe^{-bc}) + bc}{b}$$

where $W(y)$ satisfies

$$W(y)e^{W(y)} = y.$$

Use the graphical representation of $W(y)$ presented in Fig. 7.33 to obtain your answer.]

7.8 Express (7.6a) in the form

$$I = \int_1^0 \mathcal{B}(T)\frac{dT}{d\tilde{p}}d\tilde{p} + \mathcal{B}(T_s)\mathcal{T}(\tilde{p}_s)$$

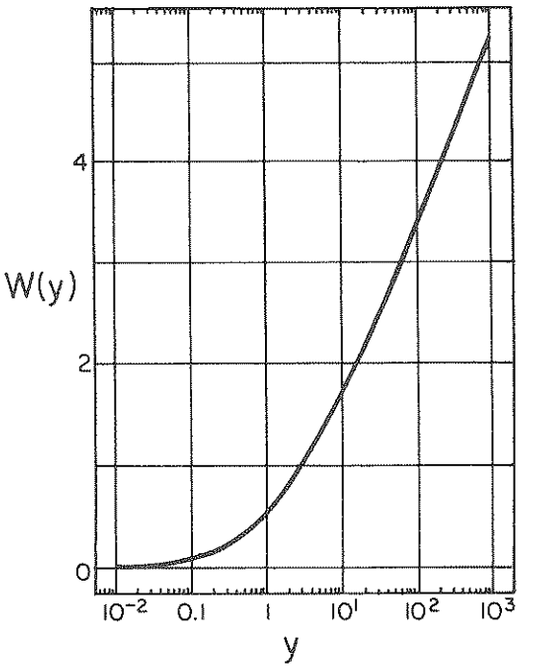

Fig. 7.33 The function $W(y)$.

assuming μ=1. Using the transmission function derived in Problem 3.7, and assuming that the Planck function varies as

$$\mathcal{B}(\tilde{p}) = \mathcal{B}^*\tilde{p}$$

where $\mathcal{B}^*$ is the blackbody function at the surface where $\tilde{p} = \tilde{p}_s = 1$, obtain the approximate solution

$$I \approx \mathcal{B}(T_s)[1 - \frac{\beta}{8} + \frac{\beta^2}{30}]$$

for $\beta < 1$ neglecting all terms $O(\beta^3)$ and above. Check the temperature corrections listed in Table 3.2 for the five values of r_s and T_s assuming $\Delta T = T_s - T^*$ where T^* is the 11μm brightness temperature $I = \mathcal{B}(T^*)$.

7.9 For an atmosphere represented by

$$p = p_o e^{-z/H}$$

estimate the ratio of the limb to vertical absorption paths for a uniformly mixed gas. Assume a tangent height h and derive an expression for the vertical path from the top of the atmosphere to this tangent height. Parameters you will need are $H = 7$ km, the radius of Earth $R = 6.37 \times 10^3$ km. Plot the ratio of the slant to vertical paths as a function of h ranging from 20 to 80 km.

7.10 Derive (7.57). You will need to consider the cloud as a thin layer located at pressure p_c and approximate the radiative transfer through this layer by (7.49).

7.11 Show that $G(p_c)$ is independent of p_c for an isothermal atmosphere.

7.12 Consider a two–layer atmosphere, the upper layer is 2km thick and contains a cloud with a mean temperature of 220 K. The lower blackbody surface has a temperature of 285 K and the intervening layer is transparent to the radiation under consideration. Using (7.55), estimate the 11μm brightness temperature observed by a radiometer on a satellite assuming $\varepsilon = 0.2$, 0.6, 0.8 and 1.0. If you assume that the lapse rate of the atmosphere is 6.5 K km^{-1}, what is the effective height of this emission?

8
Active Sensing

Active sensing is a powerful way of observing the atmosphere. Measurements from active systems are now used extensively in research as well as routinely as part of the operational observations provided by national weather services worldwide. Figure 8.1 portrays the essential elements of a generic active system. In the operation of such a system, electromagnetic energy is transmitted into the atmosphere, absorbed and scattered by the intervening aerosols and gases, and then scattered by a target volume at some determined range. The energy scattered by this volume and returned to a receiver is referred to as the echo. This echo is then processed to provide the information of interest. Two basically different modes of detection distinguish the capabilities of the system. For example, an active system might detect only the intensity of the backscattered radiation in which case the system is said to be *incoherent*. Other active systems may have detection capabilities that provide a measure of both the phase and amplitude of the backscattered electromagnetic wave. These systems, sometimes referred to as *coherent* systems, are much more complex in both their design and in their operation. Coherent systems are used, for example, to measure atmospheric motions based on measurements of the Doppler shift of the returned signal.

This chapter reviews the principles of remote sensing of two active systems: radar and lidar. Radars transmit a pulse of microwave energy to the atmosphere whereas lidars transmit shorter wavelength UV, visible, or infrared radiation. Although the design and operation of each is very different, the broad principles of remote sensing by these systems are ostensibly the same.

Figure 8.2 contrasts various operating wavelengths of lidars and radars against a typical atmospheric molecular absorption–transmission spectrum. Most weather radars operate at longer microwave wavelengths (operational weather radars operate in the S band, for example). Clear air radars, on the other hand, operate at VHF and UHF frequencies (50 MHz to 1000 MHz) with wavelengths ranging from about 30 cm to 6 m. Both systems are largely unaffected by gaseous absorption but this is not the case for radars

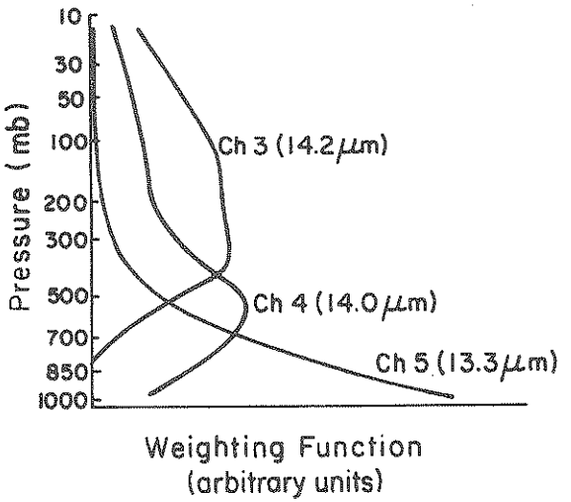

Figure 7.26 The weighting functions for three VAS CO_2 spectral bands centered at 14.2, 14.0, and 13.3 μm used in CO_2 slicing (Wylie and Menzel, 1989).

for the upwelling intensity at pressure level p. The radiation received at $p = 0$ then follows as[7]

$$I(0,\mu) = I(p,\mu)\mathcal{T}(p,0,\mu) + \int_0^p \mathcal{B}(p')\mathcal{W}(0,p')dp' \tag{7.55}$$

or in terms of the surface emission $I(p_s,\mu)$ as

$$I(0,\mu) = I(p_s,\mu)\mathcal{T}(p_s,p,\mu)\mathcal{T}(p,0,\mu) +$$

$$\mathcal{T}(p,0,\mu)\int_p^{p_s} \mathcal{B}(p')\mathcal{W}(p,p')dp' + \int_0^p \mathcal{B}(p')\mathcal{W}(0,p')dp' \tag{7.56}$$

With this form of transfer equation, it follows that the intensity difference between clear sky and a cloudy sky is

$$\Delta I = I_{clear} - I_{cldy} = \varepsilon \int_{p_s}^{p_c} \mathcal{T}(0,p')\frac{d\mathcal{B}(p')}{dp'}dp' \tag{7.57}$$

[7] There are a number of subtle assumptions in going from (7.54) to (7.56). The form of transfer equation given by (7.56) is referred to as the stacked layer equation. This is only valid when transmission functions multiply

$$\mathcal{T}(p_s,0,\mu) = \mathcal{T}(p_s,p,\mu)\mathcal{T}(p,0,\mu)$$

such as for transmission functions that are pure exponential functions of path.

where ε is the cloud emissivity and the wavelength ratio of this intensity difference defines a function

$$G(p_c) = \frac{\Delta I_1}{\Delta I_2} = \frac{\varepsilon_1 \int_{p_s}^{p_c} \mathcal{T}\frac{d\mathcal{B}_1}{dp'}dp'}{\varepsilon_2 \int_{p_s}^{p_c} \mathcal{T}\frac{d\mathcal{B}_2}{dp'}dp'}$$

that depends on cloud top pressure. This function is referred to as the cloud top pressure function and its general properties can be examined as follows. Suppose the optical depth of the atmosphere has the form

$$t(\tilde{p}) = \tau^*\tilde{p}^2 \tag{7.58}$$

which follows directly from (7.36) with $\tilde{p} = p/p_s$ and suppose also that the Planck function varies with pressure in the following simple way

$$\mathcal{B} = \mathcal{B}_o + \mathcal{B}^*\tilde{p}.$$

Substitution of (7.58) into the definition $\mathcal{T}(0,p) = \exp(-t(\tilde{p})/\mu)$ together with differentiation of the Planck function yields

$$G(p_c) = \frac{\mathcal{B}_1^* \int_{\tilde{p}_s}^{\tilde{p}_c} \tilde{p}' \exp[-\tau_1^*\tilde{p}'^2]d\tilde{p}'}{\mathcal{B}_2^* \int_{\tilde{p}_s}^{\tilde{p}_c} \tilde{p}' \exp[-\tau_2^*\tilde{p}'^2]d\tilde{p}'} \tag{7.59}$$

for $\mu = 1$. It is also convenient to assume that $\mathcal{B}_1^*/\mathcal{B}_2^* = 1$, that $\tilde{p}_s = p_s/p_o = 1$ and that the two wavelengths are close enough that $\varepsilon_1 = \varepsilon_2$. It follows from integration of (7.59) that

$$G(p_c) = \left(\frac{\tau_2^*}{\tau_1^*}\right)\frac{\exp[-\tau_1^*\tilde{p}_c^2] - \exp[-\tau_1^*]}{\exp[-\tau_2^*\tilde{p}_c^2] - \exp[-\tau_2^*]} \tag{7.60}$$

and examples of $G(p_c)$ derived from this formula are presented in Fig. 7.27a for different values of atmospheric optical depth τ_1^* and τ_2^*. The curves indicate how the cloud–top function depends on the ratio of optical depths as well as on the magnitude of these optical depths. In an optically thin atmosphere (curve 1), the function $G(p_c)$ only weakly depends on cloud–top pressure since emission by the clouds affects both channels more or less equally throughout most of the atmosphere. The other extreme is an optically thick atmosphere (curve 4) in which case the cloud–top pressure function is extremely sensitive to clouds with low cloud–top pressures. In this case, the peak of the weighting function of the optically thicker atmosphere